Chemical Geology 533 (2020) 119429

Contents lists available at ScienceDirect

Chemical Geology

journal homepage: www.elsevier.com/locate/chemgeo

SIMS oxygen isotopes indicate Phanerozoic fluids permeated a Precambrian gold deposit

Erik L. Haroldson[a,*], Philip E. Brown[a], Akizumi Ishida[a,b], John W. Valley[a]

[a] Department of Geoscience, University of Wisconsin-Madison, 1215 West Dayton Street, Madison, WI 53715, USA
[b] Department of Earth Science, Graduate School of Science, Tohoku University, Sendai 9808578, Japan

ARTICLE INFO

Editor: Catherine Chauvel

Keywords:
Oxygen isotopes
SIMS
Laser fluorination
Mississippi Valley-type
Gold
Volcanogenic massive sulfide

ABSTRACT

The Reef Deposit is an anomalous Au—Cu occurrence in the Paleoproterozoic terranes of northern Wisconsin, better known as host to significant Cu—Zn volcanogenic massive sulfide (VMS) deposits. Previous work using lead isotopes and fluid inclusions has identified a protracted development of the mineralization from initial formation as the root zone veins of a VMS deposit during the Penokean orogeny (~1.9–1.8 Ga), with the most recent mineralization/remobilization activity associated with late Paleozoic Mississippi Valley-type (MVT) fluid flow (Haroldson et al., 2018a, 2018b). Here we use the oxygen isotope history of the Reef Deposit to verify and further examine the deposit's protracted development.

Laser fluorination oxygen isotope measurements of primary mineralized quartz veins range in $\delta^{18}O$ from 6.8 to 10.0‰ (VSMOW), and a trend is observed of increasing $\delta^{18}O$ values of parallel vein zones along a 400-m traverse from northwest to southeast, likely from a temperature gradient during initial formation. Temperature estimates for a VMS deposit setting (230 to 400 °C) are consistent with a hydrothermally shifted formation fluid, using seawater $\delta^{18}O$ estimates during the Penokean Orogeny and evolving to higher $\delta^{18}O$ by incorporation of magmatic fluids or interaction with local crust.

In situ oxygen isotope measurement by Secondary Ion Mass Spectrometer (SIMS) of cross-cutting quartz and carbonate range in $\delta^{18}O$ from 19.4 to 28.4‰ for quartz, 25.3 to 28.1‰ for dolomite, and 9.6 to 29.3‰ (VSMOW) for calcite. High $\delta^{18}O$ values (> 19‰) are measured in a crustiform-textured quartz stockwork microveinlet, in dolomite observed in late carbonate microveinlets, and calcite in settings associated with the late quartz and dolomite and a separate calcite-only setting directly linked with gold mineralization/remobilization.

1. Introduction

The measurement of oxygen isotope ratios from hydrothermal ore deposits has been used as a temperature of mineralization proxy and fluid-source tracer (Ohmoto, 1986). The advent of SEM/SIMS, secondary ion mass spectrometry (SIMS) in concert with cathodoluminescent imaging by SEM, has enabled *in situ* analyses to reveal secondary hydrothermal events (Graham et al., 1996; Allan and Yardley, 2007; Cernuschi et al., 2018). Recent advances in SIMS greatly increase the spatial resolution, precision and accuracy of *in situ* measurement of quartz and carbonate gangue minerals (Valley and Kita, 2009; Śliwiński et al., 2016a).

There are several oxygen isotope studies of VMS deposits globally, but they are primarily on whole rock samples showing a regional concentric isotopic zoning pattern in the host rocks surrounding a VMS deposit (Cathles, 1993; Paradis et al., 1993; Huston and Taylor, 1999). Previous oxygen isotopic examinations of VMS deposits performed on individual mineral phases commonly analyze carbonate minerals by acid dissolution in order to also ascertain $\delta^{13}C$ information. When $\delta^{18}O$ is measured from quartz separates in VMS deposits, it is most commonly separated from host rhyolite volcanic sequences or variably altered quartz-sericite or chlorite host rocks (Lentz, 1999). Quartz veins are relatively rare in the main massive sulfides of VMS deposits and the root zones typically consist of silicified volcanic rocks and there is a general lack of discrete veins. Consequently, there are very few oxygen isotopic studies of quartz from veins associated with the primary VMS mineralization or from the root zone of a VMS deposit. MacLean and Hoy (1991) measured three quartz separates from quartz and quartz-sulfide veins associated with the Horne mine which yielded $\delta^{18}O_{Qtz}$ values of 10.2, 11.0 and 12.1‰ (SMOW).

Here we investigate the oxygen isotope geochemistry of the Au—Cu Reef Deposit in northern Wisconsin. The Reef Deposit occurrence was

* Corresponding author at: Department of Geosciences, Austin Peay State University, P.O. Box 4418, Clarksville, TN 37044, USA.
E-mail address: haroldsone@apsu.edu (E.L. Haroldson).

https://doi.org/10.1016/j.chemgeo.2019.119429
Received 31 July 2019; Received in revised form 7 November 2019; Accepted 22 November 2019
Available online 26 November 2019

discovered in the 1970's during exploration for Cu−Zn volcanogenic massive sulfide (VMS) deposits in the region. The geologic development of the deposit involves initial mineralization as the root zone of a VMS deposit during the Paleoproterozoic (~1870 Ma), and ~1.5 b.y. later, was subject to overprinting gold mineralization/remobilization during the late Paleozoic, by Mississippi Valley-type fluids (Haroldson et al., 2018a). Mineralization/remobilization is also assumed to have occurred during regional metamorphism in the last stages of the Penokean orogeny (~1835 to 1830 Ma). As well, it is observed that alteration of pyrite into the extensive amounts of pyrrhotite found in the Reef Deposit, along with possible gold mineralization/remobilization was caused by a reduced CH_4-bearing fluid associated with emplacement of the adjacent Wolf River Batholith ~1475 Ma (Haroldson et al., 2018b).

In this study, bulk samples of mineral separates from primary quartz veins are measured at mm-scale using conventional laser fluorination/gas-source mass spectrometry analyses which identify temperature and source fluid constraints for the primary VMS mineralization. *In situ* SIMS analyses at μm-scale of small cross-cutting quartz and carbonate minerals identifies uniquely different variable isotopic signatures, representative of the latest overprinting MVT event.

High-$\delta^{18}O$ measurements of quartz overgrowths and carbonate cements in Paleozoic sedimentary units located as close as 50 km to the south have been observed, sometimes with portions interpreted to be associated with through-going flow of Mississippi Valley-type (MVT) fluids (Pollington et al., 2011; Hyodo et al., 2014; Śliwiński et al., 2016b; Pollington et al., 2016). Similarities in $\delta^{18}O$ measurements and mineral growth textures are further evidence for MVT fluids infiltrating the Reef Deposit.

Secondary fluids, identified in calcite- and quartz-hosted secondary fluid inclusions in the Reef Deposit, are variably saline (Haroldson et al., 2018b). The effect of salinity on fractionation of $\delta^{18}O$, known as the *salt effect*, has been studied for some time (Truesdell, 1974; O'Neil and Truesdell, 1991; Horita et al., 1993a, 1993b; Horita et al., 1995; Driesner and Seward, 2000; Hu and Clayton, 2003). Salinities of 23.6 to 24.7 wt% NaCl equivalent, reported for the calcite-hosted fluid inclusions, would require other cations such as K, Ca or Fe, in addition to Na, to explain a lack of halite daughter salts present at room temperature (Haroldson et al., 2018b). The evidence is for greater *salt effect* fractionation involving divalent cations (Horita et al., 1993a). In any case, the salt effect does not appear to alter the isotopic system by more than ~2‰ even at low temperatures (O'Neil and Truesdell, 1991). Although the precision of temperature estimates is limited, this does not significantly affect our interpretations, therefore for simplicity, we report $\delta^{18}O_{Qtz}$, $\delta^{18}O_{Cc}$ and $\delta^{18}O_{Dol}$ temperature estimates without correcting for a possible *salt effect*.

2. Geology

The Precambrian Wisconsin magmatic terranes are found near surface in Northern Wisconsin and Upper Peninsula Michigan where Paleozoic sedimentary rock cover has been eroded, albeit significant portions of these terranes are now overlain by glacial overburden (Fig. 1). The terrane, also referred to as the "Penokean terrane", formed during the Penokean orogeny (1890 to 1830 Ma, Schulz and Cannon, 2007), part of the Trans-Hudson orogeny. During the Penokean orogeny, multiple volcanic-arc sequences docked onto the southern Archean-aged Superior Province, and those arcs were later thrusted further onto the Superior Province from the south (modern direction), by the accretion of a smaller Archean-aged craton known as the Marshfield terrane (Schulz and Cannon, 2007). Two prominent volcanic arc terranes are identified within the Pembine Wausau Subterrane. The older (1890 to 1860 Ma) terrane, referred to as the Ladysmith Rhinelander Volcanic Complex, is host to several Cu−Zn VMS deposits (Fig. 1) (DeMatties, 1996). The younger (1845 to 1835 Ma; LaBerge and Myers, 1984) terrane is adjacent to the south and known as the Wausau Volcanic Complex (WVC). The WVC is only known to host minor Cu−Zn type occurrences, as well as the Au−Cu occurrence known as the Reef Deposit (Fig. 1) (Haroldson et al., 2018a, 2018b).

The Reef Deposit does not outcrop on surface, and the geology is only known through mineral exploration drill holes, none of which are oriented for structural measurements. The deposit formed initially during the Penokean orogeny time frame, likely as the root zone of a VMS deposit, or potentially in an orogenic gold setting (Kennedy and Harding, 1990; Haroldson et al., 2018b). Mineralized zones are hosted in a 300–700 m wide zone of deformation. This deformation makes identification of the host rock protolith difficult, and the largely mafic host rocks within this zone are referred to as "granofels" (Fig. 2a) (Kennedy and Harding, 1990). The deformation zone is also host to several felsic intrusions with unknown affinity, although a close spatial relationship with multiple mineralized zones suggests a possible genetic link. Outside the deformation zone, the area is flanked to the west by 1845 to 1835 Ma Wausau Volcanic Complex rocks, primarily consisting of massive and pillowed basaltic flows, mafic tuffs and gabbro intrusions (Fig. 2a) (Kennedy and Harding, 1990). Immediately adjacent to the east of the deposit is the 1484 to 1468 Ma Wolf River Batholith (Fig. 2a), formed during a magmatic episode which emplaced a belt of "anorogenic" intrusions that runs from southern California, USA to Labrador, Canada (Anderson, 1983; Dewane and Van Schmus, 2007). The deposit is directly overlain by a < 5–40 m thick saprolite and regolith zone, likely formed during Precambrian weathering (Driese and Medaris, 2008; Fig. 2b).

Eight Au−Cu mineralized quartz-sulfide vein zones have been identified and modelled (labelled by single alphabetical characters: A–F, Q and X) for the Reef Deposit (Kennedy and Harding, 1990) (Fig. 2). Quartz veins contain abundant chlorite filled fractures (Fig. 3a). The most abundant sulfide mineral is pyrrhotite, observed in veins and disseminated in wall-rock along with chalcopyrite and pyrite (Fig. 3b). Local carbonate veinlets and microveinlets are observed cross-cutting the host granofels (Fig. 3c) and primary quartz veins (Fig. 3d). Alteration minerals, chlorite, biotite, tremolite and sericite, are commonly associated with the primary mineralized zones. The sulfides are pyrrhotite, pyrite and chalcopyrite; magnetite is relatively less common and molybdenite, sphalerite and galena are rarely observed (Kennedy and Harding, 1990; Haroldson et al., 2018a, 2018b). Gold grains are small, only rarely observed at the hand lens scale and are found in two primary textural settings by detailed scanning electron microscopy (Haroldson et al., 2018a). Gold in the first textural setting is hosted in pyrite and interpreted to be associated with the VMS-stage mineralization. Gold in the second textural setting is found along quartz and sulfide microfractures and grain boundaries indicating later mineralization/remobilization. Gold is observed as native gold and in the telluride minerals petzite (Ag_3AuTe_2) and calaverite ($AuTe_2$). Altaite (PbTe), telluro-bismuthite ($BiTe_3$), hessite (Ag_2Te), melonite (NiTe) and frohbergite (FeTe) are observed associated with native gold and gold telluride minerals.

The host rocks and mineralized zones were metamorphosed and deformed during regional metamorphism associated with the Penokean orogeny (Haroldson et al., 2018b). Haroldson et al., 2018b observed evidence consistent with amphibolite facies metamorphism, indicated by aluminous hornblende and plagioclase mineralogy, the results of neonate fluid inclusion microthermometry, and quartz grain boundary migration recrystallization (GBR) textures (Stipp et al., 2002a, 2002b). A general lack of carbonate in quartz veins of the Reef Deposit, and the presence of deformed garnet-bearing and epidote-bearing (non-Au-mineralized) veins has been viewed as evidence for complete alteration of primary carbonates during regional deformation (Kennedy and Harding, 1990). The calcite microveinlets and calcite-dolomite veinlets observed in this study cross-cut the primary veins and do not show any alteration and deformation textures that would be expected from amphibolite grade metamorphism. Therefore, local cross-cutting dolomite-calcite bearing microfractures and veinlets, which are the subject of much of the analysis in this report, were formed post regional

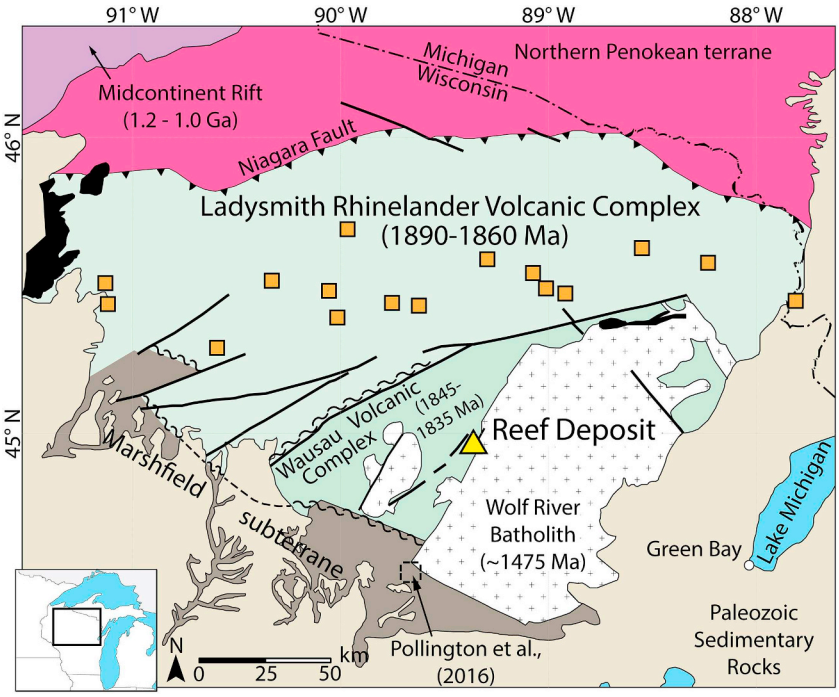

Fig. 1. Simplified geologic map (modified from Haroldson et al., 201b8) of Pembine-Wausau subterrane (includes Ladysmith Rhinelander Volcanic Complex and Wausau Volcanic Complex) and surrounding area. Triangle - the Reef Deposit, squares - volcanogenic massive sulfide deposits. Solid lines represent faults, squiggly lines represent shear zones. Black lithology areas represent Proterozoic quartzite, the dark grey Marshfield subterrane is Archean in age. The location of outcrop A from Pollington et al. (2016) is identified.

deformation (Haroldson et al., 2018a, 2018b).

3. Methods

Seventeen samples were selected from Reef Deposit NQ (47.6 mm diameter) drill cores, owned by Aquila Resources Inc. and housed in facilities in Upper Peninsula Michigan. The sampling selection represents the vertical and horizontal extents of all mineralized zones modelled by Kennedy and Harding (1990). Samples analyzed in this study are curated in the University of Wisconsin-Madison Geology Museum (UW# 2034; Haroldson, 2017). One sample was selected from a barren quartz vein that cross-cuts the footwall gabbro, a unit that itself cross-cuts mineralized zones. Four felsic intrusive samples were selected with the goal of sampling the least altered rocks, which consequently were two samples from a felsic intrusion on the west side of the granofels zone, and two samples from intrusions found in drill holes at depth on the east side of the deposit (not the Wolf River Batholith). Quarter core sample sections were separated using a diamond saw.

Oxygen isotope analyses of bulk chips (approximately 2 mg) of the Reef Deposit quartz veins were conducted in the Stable Isotope Laboratory at the Department of Geoscience, University of Wisconsin-Madison using a laser fluorination extraction line and a Finnigan MAT 251 mass spectrometer (Spicuzza et al., 1998). The garnet standard (UWG-2, $\delta^{18}O$ = 5.80‰ Vienna standard mean ocean water (VSMOW), Valley et al., 1995) was analyzed before and after the quartz sample measurements. The reproducibility of the UWG-2 standard by laser fluorination (1SD; standard deviation) is approximately 0.1‰ for $\delta^{18}O$ (Spicuzza et al., 1998). All $\delta^{18}O$ results refer to VSMOW.

Samples selected for *in situ* $\delta^{18}O$ measurement were cut using a slow speed diamond saw and cast into 2 separate 25-mm-diameter epoxy mounts, positioning areas of interest within a 5-mm radius of the geometric center, to minimize potential fractionation effects related to the focusing axis within the SIMS analysis chamber (Kita et al., 2009; Valley and Kita, 2009). For the carbonate sample mount (RC01), multiple grains of a running calcite standard (UWC-3, $\delta^{18}O$ = 12.49‰ (VSMOW), Kozdon et al., 2009) were embedded in the center. Similarly for the quartz sample mount (R4799), multiple grains of a running quartz standard (UWQ-1, $\delta^{18}O$ = 12.33‰ (VSMOW), Kelly et al., 2007) were embedded in the center. Small variation in the topographic relief of the prepared sample may cause deformation of the local electrostatic field applied on the surface of the sample, which deviates the trajectory of secondary ions of individual isotopes, degrading precision of the measurement (Kita et al., 2009). Mounts were polished to a 0.25 μm finish, and with the carbonate sample in particular, care was taken to keep polishing relief between the quartz and carbonate to less than a few micrometers. After cleaning in deionized water and ethyl alcohol, mounts were carbon coated with a thickness of ~20 nm.

Imaging was performed on a Hitachi S3400−N Scanning Electron Microscope (SEM) at the Ray and Mary Wilcox Scanning Electron Microscopy Laboratory, Department of Geoscience, University of Wisconsin-Madison using Secondary Electron (SE), Back Scattered Electron (BSE) and Cathodoluminescence (CL) detectors.

In situ $\delta^{18}O$ measurements were performed by SIMS at the Wisconsin Secondary Ion Mass Spectrometer (WiscSIMS) Laboratory, Department of Geoscience, University of Wisconsin-Madison using a CAMECA IMS 1280 large-radius multicollector ion microprobe. Sample data were collected during one 12-h session on January 27, 2017. Four consecutive measurements of either UWC-3 (carbonate bracket) or UWQ-1 (quartz bracket) standard were performed before and after every 10–15 sample analyses. The full data set is provided in appendix A. Instrumental conditions were similar to those of Śliwiński et al. (2016a, 2016b); a 10 keV, 1.3–1.4 nA primary beam of $^{133}Cs^+$ ions was focused to a ~12 μm diameter on the sample surface. The depth of the sputtered sample pits was ~1 μm. Charge neutralization of the carbon coated samples was aided by using an electron flood gun. Count-rates of oxygen ions ($^{18}O^-$ and $^{16}O^-$) were collected simultaneously by two Faraday cup detectors (H1 and C, respectively), with a mass resolving power of 2500 for ^{18}O and ^{16}O. Typical secondary $^{16}O^-$ ion intensity were ~2.0 × 10^9 cps/nA for carbonate and ~1.5 × 10^9 cps/nA for quartz. Individual analyses took ~4 min including ~10 s of pre-sputtering through the carbon coat, ~60 s of automatic re-centering of secondary ions in the field aperture, and 80 s of oxygen isotope measurements (20 cycles of 4 s integrations). The intensity of $^{16}O^1H$ was measured simultaneously and the background-corrected ratios of $^{16}O^1H/^{16}O$ (Wang et al., 2014) are used to monitor individual analyses for possible hydrous contamination. All *in situ* SIMS results refer to VSMOW.

Accuracy of SIMS $\delta^{18}O$ measurements are affected by instrumental

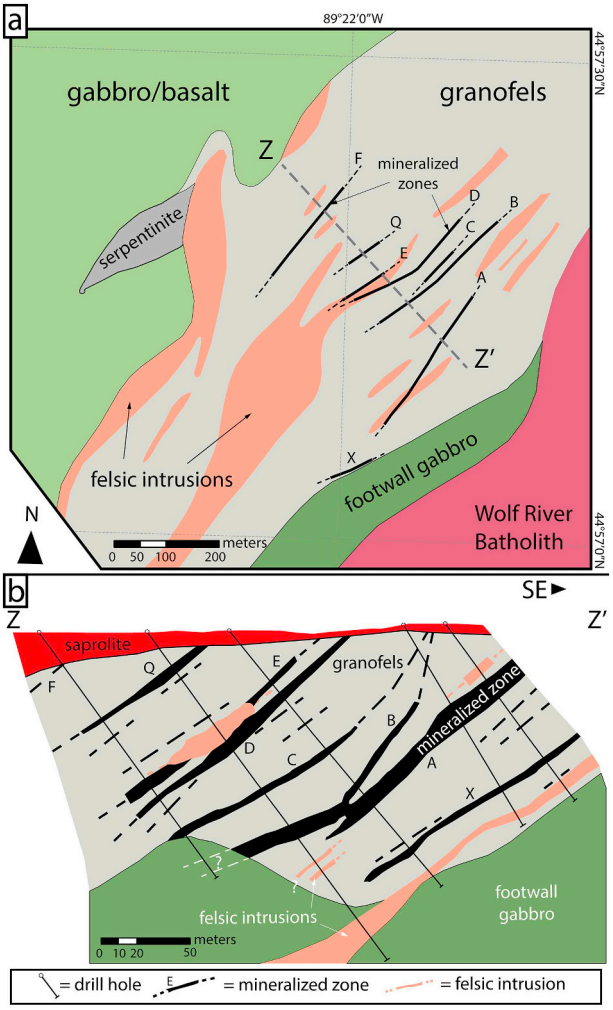

Fig. 2. (a) Bedrock geologic map of the Reef Deposit projected to surface from drill hole data, after Kennedy and Harding (1990). Mineralized zones are identified by single alphabetic characters (A–F, Q and X). Dashed line (Z-Z′) identifies location of cross-section in panel b. (b) Representative geologic cross-section of the Reef Deposit looking northeast, showing orientation of mineralized zones and geometry of footwall gabbro unit at depth which cross-cuts mineralized zones. Black – mineralized zones, black dashes - minor mineralization, salmon– felsic intrusions, burgundy– Wolf River Batholith, grey – granofels (see text for definition), light green – relatively unaltered gabbro/basalt of the Wausau volcanic complex, dark green – footwall gabbro, red – saprolite. (For interpretation of the references to colour in this figure legend, the reader is referred to the web version of this article.)

Fig. 3. Photographs showing mineralized quartz veins and cross-cutting carbonate veins in the Reef Deposit. (a) Typical quartz vein with sulfide and chlorite-filled fractures. (b) Semi-massive sulfide consisting primarily of pyrrhotite with minor pyrite. (c) Carbonate (calcite, dolomite) veinlet cross-cutting the host granofels. (d) Carbonate (calcite, dolomite) veinlet cross-cutting a primary quartz vein.

mass fractionation of which a component is systematically related to the chemical composition and crystal structure of the sample (matrix effect, Hervig et al., 1992; Kita et al., 2009; Valley and Kita, 2009). For dolomite-ankerite solid solutions, we employed a calibration scheme developed for carbonate minerals using a suite of standards for correcting SIMS $\delta^{18}O$ bias (Śliwiński et al., 2016a). Chemical analyses were performed by EPMA in the immediate vicinity of and within the same imaged CL intensity domain of SIMS pits using a CAMECA SX-51 in the Eugene N. Cameron Electron Microprobe Laboratory, Department of Geoscience, University of Wisconsin-Madison. The analytical precision (spot to spot) of SIMS analysis was between 0.15 and 0.25‰ (2 SD). All SIMS data are reported in Table DR-1.

Estimates for the temperature of precipitation are made using fractionation equations from Sharp et al. (2016) for quartz ($1000 \ln \alpha_{Qtz\text{-}H2O} = 4.28(0.07) \times 10^6 T^{-2} - 3.5(0.2) \times 1000 T^{-1}$), Horita (2014) for dolomite ($1000 \ln \alpha_{Dol\text{-}H2O} = 3.140(0.022) \times 10^6 T^{-2} - 3.14(0.11)$) and Friedman and O'Neil (1977) after O'Neil et al. (1969) for calcite ($1000 \ln \alpha_{Cc\text{-}H2O} = 2.78 \times 10^6 T^{-2} - 2.89$).

4. Results

4.1. Dolomite zonation

Gangue dolomite in the Reef Deposit has euhedral open-space growth textures found in late cross-cutting carbonate veinlets (Fig. 4). Four distinctive zones are identified using petrography and CL imaging. The inner zone (zone 1) is cloudy in plane polarized light, and has a moderate to bright luminescence with a mottled texture. Zone 2 forms a small band of mottled texture dolomite (similar to zone 1) in CL, with a slightly darker luminescence. Zone 3 is characterized by sharply defined concentric banding, overall this zone has the brightest luminescence. A major dissolution surface occurs on the outside of zone 3, prior to zone 4 growth. Zone 4 also displays concentric zoning and is dull to non-luminescent. Small (< 200 μm) clusters of chalcopyrite with an unusual acicular, bladed habit are observed on outer surfaces of zone 4 dolomite, preceding an irregular dissolution surface of zone 4 dolomite and the growth of void-filling calcite.

4.2. Bulk analyses

Laser fluorination $\delta^{18}O$ measurements of quartz grains from Reef Deposit quartz veins and felsic intrusions are reported in Table 1. Results from mineralized vein quartz samples are shown in Fig. 5. The measured values of mineralized quartz veins range from 6.8‰ to 10.0‰. The quartz vein which cross-cuts the footwall gabbro unit has a measured $\delta^{18}O$ of 7.3‰. Measurements of quartz from the four felsic intrusive samples show a small range in $\delta^{18}O$ from 7.7 to 8.2‰.

4.3. In situ analyses

SIMS *in situ* oxygen isotope measurements are reported in Table 2 and Fig. 6. Measurements of $\delta^{18}O$ were made of quartz in primary

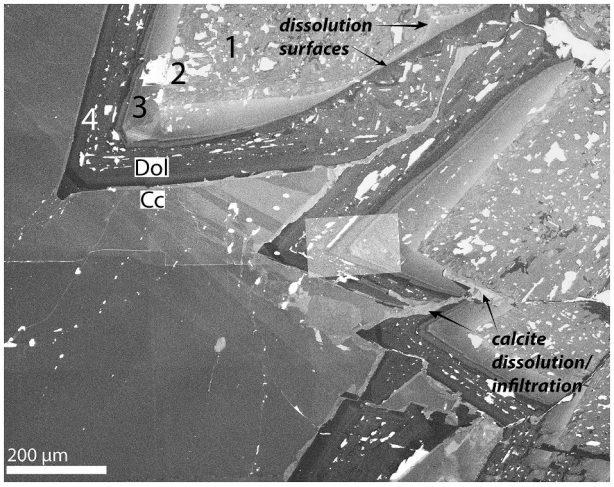

Fig. 4. Cathodoluminescence (CL) image of dolomite (Dol) and calcite (Cc) textures observed in a 10 cm wide carbonate veinlet in sample EH1512. Dolomite growth zones (1–4) discussed in the text are identified. Dissolution surfaces on zones 2 and 3 are identified in the top center portion of the image. Calcite formed along a dissolution surface of zone 4 dolomite and infiltrated along fractures to interior of dolomite. Calcite has concentric zoning in places. Bright areas are related to pits from rough polish of carbonates, due to edge effects or from polishing-powder filling pits. Image is made from composite of multiple images. Small grey area in center was taken later to remove dirt on sample, with slightly different machine settings used.

Table 1
Laser fluorination oxygen isotope measurements.

Sample	Zone	$\delta^{18}O_{Qtz}$ (‰) VSMOW
Mineralized vein quartz		
09A	X	9.37
09B	X	9.34
35	X	9.97
8	X	9.03
31	X	9.67
1	A	9.46
12	A	8.56
30A	A	8.74
30B	A	8.72
32	A	9.25
02A	B	8.25
02B	B	8.70
3	C	8.13
04A	D	8.34
04B	D	8.30
05A	D	7.87
05B	D	7.68
36	D	8.26
37	D	7.91
06A	E	8.55
06B	E	8.36
7	F	6.84
Post-mineral vein quartz[a]		
11	n/a	7.26
Felsic intrusion quartz		
19	n/a	7.74
20	n/a	8.14
21	n/a	8.19
22	n/a	7.78

[a] Vein cross-cuts footwall gabbro, clearly post-dating primary mineralization.

quartz veins and cross-cutting crustiform and void-filling texture quartz, carbonate (calcite and dolomite) veinlets that cross-cut the primary quartz veins, as well as, disseminated calcite found locally replacing pyrrhotite. The SIMS measurements range in $\delta^{18}O$ from 8.5 to

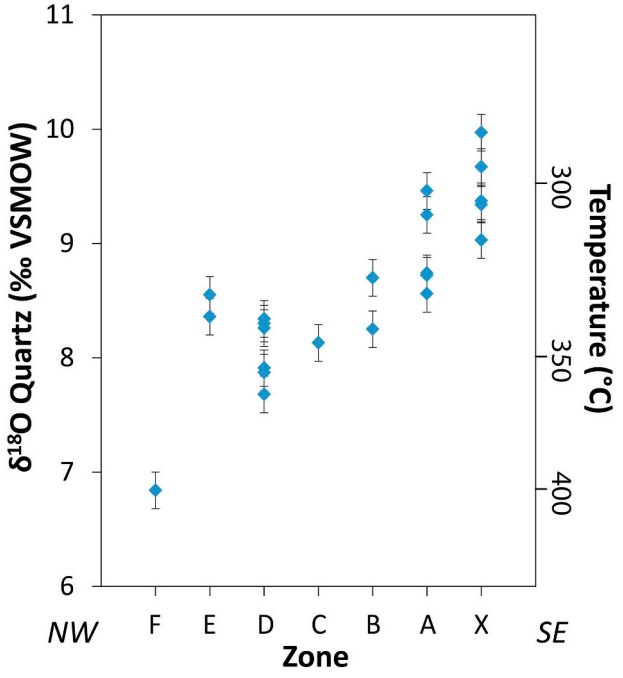

Fig. 5. Oxygen isotope compositions of mineralized quartz veins measured on quartz separates by laser fluorination. Results are sorted by individual vein zones occurring from northwest to southeast (Fig. 3) depicted as left to right in the figure. Temperature estimates assume precipitation in equilibrium with hydrothermally shifted Paleoproterozoic seawater (2.6‰ VSMOW assuming no variation during the primary mineralization) and quartz-water fractionation ($1000 \ln \alpha = 4.28(0.07) \times 10^6 T^{-2} - 3.5(0.2) \times 1000 T^{-1}$) from Sharp et al. (2016).

28.4‰ for quartz, 25.3 to 28.1‰ for dolomite, and 9.6 to 29.3‰ for calcite. High $\delta^{18}O$ values (> 19‰) are found in quartz and carbonate cross-cutting and replacement features, at times, in direct contact of primary vein quartz which give relatively low $\delta^{18}O$ values (8 to 13‰ range) when measured by SIMS.

Stockwork veinlets with crustiform, successively banded, and void-filling euhedral quartz are 10 µm to 0.5 cm wide and cross-cut the primary quartz veins (Fig. 7, DR-4). The crustiform texture and concentric zoning of euhedral crystal growth is only visible in CL. The veinlets also contain chlorite and sulfides (pyrite and chalcopyrite) with final void filling by calcite. Chalcopyrite mineralization/remobilization has been associated with fluid circulation driven by Wolf River Batholith emplacement (Haroldson et al., 2018b). Chalcopyrite is also identified in MVT deposits (Leach et al., 2010), and in late carbonate veinlets in this study (see Section 5.3.3). A transect of SIMS analyses across the crustiform growth quartz reveals $\delta^{18}O_{Qtz}$ values that vary from 19.4‰ to 28.4‰. There is a general decrease in $\delta^{18}O_{Qtz}$ from the veinlet selvage towards the center, with a return to heavier $\delta^{18}O_{Qtz}$ in the brighter CL quartz found in the center of the veinlet. Late calcite fill in this setting is discussed in Section 5.3.4.

Measurements of $\delta^{18}O_{Qtz}$ in the immediately adjacent primary vein quartz, on either side of the crustiform veinlet show no exchange with the host primary quartz. Two laser fluorination measurements from the particular sample (sample 09) gave $\delta^{18}O_{Qtz}$ values of 9.37 and 9.34‰ and the SIMS analyses in the primary quartz of the corresponding sample measured $\delta^{18}O_{Qtz}$ values of 9.0‰ (Fig. 7b). Any exchange at low temperature would shift the primary quartz towards the heavier $\delta^{18}O$ values. Further examination of quartz textures in proximity of the crustiform quartz veinlet was performed using SIMS (results are depicted in figure DR-1). As well, curious dark CL quartz growth zones observed along quartz and sulfide grain boundaries, consistent with later quartz growth, were examined by SIMS (results are depicted in

Table 2
Results of *in situ* oxygen isotope analyses of Reef Deposit quartz, calcite and dolomite using secondary ion mass spectrometry and EPMA.

Sample	Session specific sample identification	Sample/spot identification	$\delta^{18}O$ (‰) VSMOW	2SD (ext.)	Mineralogy	$\%MgCO_3$	$\%CaCO_3$	$\%MnCO_3$	$\%FeCO_3$	$^{1}Fe\#$
Sample EH1512 transect from calcite and across dolomite zoning area A										
	723	RC01 1512 c A01	27.06	0.19	Cal	1.04	97.84	0.81	0.31	–
	724	RC01 1512 c A02	24.41	0.19	Cal	1.12	96.95	1.50	0.43	–
	725	RC01 1512 c A03	25.72	0.19	Cal	0.89	97.93	0.96	0.22	–
	726	RC01 1512 c A04	25.65	0.19	Cal	0.92	97.92	0.90	0.27	–
	727	RC01 1512 d A05	25.25	0.19	Dol	42.38	51.66	1.68	4.28	0.092
	728	RC01 1512 d A06	27.19	0.19	Dol	47.13	50.42	0.64	1.81	0.037
	729	RC01 1512 d A07	27.61	0.19	Dol	46.47	51.28	0.58	1.67	0.035
	730	RC01 1512 d A08	26.60	0.19	Dol	46.39	51.04	1.74	0.83	0.018
	731	RC01 1512 d A09	28.09	0.19	Dol	47.83	50.42	1.40	0.36	0.007
	732	RC01 1512 d A10	27.06	0.19	Dol	46.89	50.19	2.58	0.34	0.007
	733	RC01 1512 d A11	27.36	0.19	Dol	47.41	50.49	1.81	0.29	0.006
	734	RC01 1512 d A12	26.95	0.19	Dol	46.74	50.51	2.46	0.29	0.006
	735	RC01 1512 d A13	27.17	0.19	Dol	46.76	50.49	2.46	0.30	0.006
Sample EH1512 transect from calcite and across dolomite zoning area B										
	853	RC01 1512 c B49	29.12	0.22	Cal	0.33	98.36	1.01	0.30	–
	854	RC01 1512 d B50	26.64	0.22	Dol	45.02	51.29	0.34	3.35	0.069
	855	RC01 1512 d B51	27.99	0.22	Dol	47.27	50.02	0.83	1.89	0.038
	856	RC01 1512 d B52	28.00	0.22	Dol	46.87	50.19	0.79	2.15	0.044
	857	RC01 1512 d B53	26.62	0.22	Dol	47.55	50.18	1.96	0.30	0.006
	858	RC01 1512 d B54	25.83	0.22	Dol	47.35	50.87	1.38	0.39	0.008
	859	RC01 1512 d B55	26.44	0.22	Dol	47.43	49.71	2.25	0.61	0.013
	860	RC01 1512 d B56	27.24	0.22	Dol	46.46	51.15	2.01	0.38	0.008
Sample EH1512 analysis of calcite and calcite twins										
	751	RC01 1512 c B25	29.27	0.18	Cal	0.05	99.47	0.48	0.00	–
	752	RC01 1512 c B26	28.49	0.18	Cal	0.20	99.06	0.63	0.12	–
	753	RC01 1512 c B27	29.00	0.18	Cal	0.59	97.75	1.34	0.32	–
	849	RC01 1512 c B45	24.82	0.22	Cal	0.13	99.50	0.15	0.21	–
	850	RC01 1512 c B46	29.28	0.22	Cal	0.65	97.72	1.32	0.30	–
	851	RC01 1512 c B47	27.86	0.22	Cal	0.24	99.07	0.61	0.09	–
	852	RC01 1512 c B48	29.29	0.22	Cal	0.75	97.52	1.53	0.20	–
Sample EH1505 100 um calcite veinlet with 2 BSE zones ($\%FeCO_3 < 1.5$)										
	747	RC01 1505 c A21	19.99	0.18	Cal	0.00	100.08	0.00	0.00	–
	741	RC01 1505 c A15	9.89	0.18	Cal	0.00	100.00	0.00	0.00	–
	769	RC01 1505 c B39	10.09	0.15	Cal	0.00	100.06	0.00	0.00	–
	771	RC01 1505 c B41	10.82	0.15	Cal	0.00	100.09	0.00	0.00	–
	748	RC01 1505 c A22	20.59	0.18	Cal	0.00	100.08	0.00	0.02	–
	750	RC01 1505 c B24	13.32	0.18	Cal	0.00	100.02	0.00	0.13	–
Sample EH1505 100 um calcite veinlet with 2 BSE zones ($\%FeCO_3 > 1.5$)										
	744	RC01 1505 c A18	9.61	0.18	Cal	0.58	97.82	0.00	1.67	–
	770	RC01 1505 c B40	23.77	0.15	Cal	0.06	93.89	3.76	2.30	–
	745	RC01 1505 c A19	23.80	0.18	Cal	0.08	94.61	2.31	3.00	–
	740	RC01 1505 c A14	24.24	0.18	Cal	0.12	92.95	3.92	3.00	–
	742	RC01 1505 c A16	22.99	0.18	Cal	0.10	91.13	4.57	4.20	–
	743	RC01 1505 c A17	22.61	0.18	Cal	0.10	91.13	4.57	4.20	–
Sample EH1509 calcite in-filling the crustiform quartz vein										
	762	RC01 1509 c A32	21.00	0.15	Cal	0.06	98.85	0.34	0.75	–
	763	RC01 1509 c A33	20.29	0.15	Cal	0.00	98.85	0.36	0.79	–
	764	RC01 1509 c A34	20.59	0.15	Cal	0.06	96.99	1.07	1.88	–
	765	RC01 1509 c B35	22.08	0.15	Cal	0.11	96.62	1.19	2.08	–
	766	RC01 1509 c B36	22.13	0.15	Cal	0.00	97.00	1.11	1.89	–
	767	RC01 1509 c B37	21.47	0.15	Cal	0.00	96.61	1.33	2.05	–
Sample EH1530 pyrrhotite replacing calcite in large patches associated with radiogenic MVT Pb isotopes (Haroldson et al., 2018a										
	758	RC01 1530 c 28	20.50	0.15	Cal	0.18	99.27	0.49	0.06	–
	759	RC01 1530 c 29	28.12	0.15	Cal	0.75	97.46	0.74	1.04	–
	760	RC01 1530 c 30	24.36	0.15	Cal	0.12	99.88	0.00	0.00	–
	761	RC01 1530 c 31	29.34	0.15	Cal	0.22	98.65	0.74	0.38	–
	846	RC01 1530 c 42	21.04	0.22	Cal	0.19	99.80	0.01	0.00	–
	847	RC01 1530 c 43	21.83	0.22	Cal	0.55	98.70	0.49	0.26	–
	848	RC01 1530 c 44	21.62	0.22	Cal	0.42	99.46	0.09	0.03	–
Sample EH1509 quartz Transect across crustiform texture veinlet										

(*continued on next page*)

Table 2 (*continued*)

Sample	Session specific sample identification	Sample/spot identification	$\delta^{18}O$ (‰) VSMOW	2SD (ext.)	Mineralogy	$\%MgCO_3$	$\%CaCO_3$	$\%MnCO_3$	$\%FeCO_3$	$^1Fe\#$
	785	R4799 1509-03 PS01	8.95	0.19	Qtz	–	–	–	–	–
	786	R4799 1509-03 PS02	28.03	0.19	Qtz	–	–	–	–	–
	787	R4799 1509-03 PS03	24.69	0.19	Qtz	–	–	–	–	–
	788	R4799 1509-03 PS04	24.46	0.19	Qtz	–	–	–	–	–
	789	R4799 1509-03 PS05	21.69	0.19	Qtz	–	–	–	–	–
	790	R4799 1509-03 PS06	26.08	0.19	Qtz	–	–	–	–	–
	791	R4799 1509-03 PS07	19.43	0.19	Qtz	–	–	–	–	–
	792	R4799 1509-03 PS08	24.75	0.19	Qtz	–	–	–	–	–
	793	R4799 1509-03 PS09	26.36	0.19	Qtz	–	–	–	–	–
	794	R4799 1509-03 PS10	28.38	0.19	Qtz	–	–	–	–	–
	795	R4799 1509-03 PS11	8.98	0.19	Qtz	–	–	–	–	–
Transect into crustiform texture veinlet closer to pyrite										
	796	R4799 1509-03 FI12	9.08	0.19	Qtz	–	–	–	–	–
	797	R4799 1509-03 PS13	25.58	0.19	Qtz	–	–	–	–	–
	798	R4799 1509-03 PS14	26.27	0.19	Qtz	–	–	–	–	–
	799	R4799 1509-03 PS15	25.69	0.19	Qtz	–	–	–	–	–
Stretch mark investigation										
	804	R4799 1509-03 SP16	9.08	0.25	Qtz	–	–	–	–	–
	805	R4799 1509-03 SP17	8.99	0.25	Qtz	–	–	–	–	–
Various analyses of crustiform vein and zoned euhedral open space growth quartz										
	826	R4799 1509-03 q CS34	8.88	0.21	Qtz	–	–	–	–	–
	827	R4799 1509-03 q CS35	27.08	0.21	Qtz	–	–	–	–	–
	828	R4799 1509-03 q CS36	25.36	0.21	Qtz	–	–	–	–	–
	829	R4799 1509-03 q CS37	26.35	0.21	Qtz	–	–	–	–	–
	830	R4799 1509-03 q CS38	25.46	0.21	Qtz	–	–	–	–	–
	831	R4799 1509-03 q CS39	22.35	0.21	Qtz	–	–	–	–	–
Sample EH1504 dark quartz areas texturally associated with gold										
	806	R4799 1504 q CS18	9.16	0.25	Qtz	–	–	–	–	–
	807	R4799 1504 q CS19	9.63	0.25	Qtz	–	–	–	–	–
	808	R4799 1504 q CS20	9.32	0.25	Qtz	–	–	–	–	–
	809	R4799 1504 q CS21	8.88	0.25	Qtz	–	–	–	–	–
	810	R4799 1504 q CS22	8.48	0.25	Qtz	–	–	–	–	–
	811	R4799 1504 q CS23	8.80	0.25	Qtz	–	–	–	–	–
	812	R4799 1504 q CS24	8.87	0.25	Qtz	–	–	–	–	–
	813	R4799 1504 q CS25	9.33	0.25	Qtz	–	–	–	–	–
	814	R4799 1504 q CS26	9.68	0.25	Qtz	–	–	–	–	–
	815	R4799 1504 q CS27	8.66	0.25	Qtz	–	–	–	–	–
Quartz inclusion in sulfide with darker CL overgrowth texturally associated with gold										
	820	R4799 1504 q ES28	8.05	0.21	Qtz	–	–	–	–	–
	821	R4799 1504 q ES29	7.93	0.21	Qtz	–	–	–	–	–
	822	R4799 1504 q ES30	8.16	0.21	Qtz	–	–	–	–	–
	823	R4799 1504 q ES31	8.30	0.21	Qtz	–	–	–	–	–
Sample EH1507 testing light and dark CL areas										
	824	R4799 1507 q 32	7.22	0.21	Qtz	–	–	–	–	–
	825	R4799 1507 q 33	7.51	0.21	Qtz	–	–	–	–	–

$^1Fe\# = FeCO_3/FeCO_3 + MgCO_3$; reported for dolomite measurements in which Fe# was used in the SIMS bias correction.

figures DR-2 and DR-3). Apart from the crustiform veinlet, no other evidence for high $\delta^{18}O_{Qtz}$ was observed.

In situ $\delta^{18}O_{Dol}$ and major element EPMA analysis of dolomite in the Reef Deposit is depicted in Fig. 8. The $\delta^{18}O$ values measured in dolomite are high, within a range from 25.3 to 28.1‰. Luminescence appears to be related to Mn concentration acting as a CL activator, and the dull to non-luminescence, seen in zone 4, due to presence of increased Fe content which acts as a CL quencher (Fig. 8) (Pierson, 1981).

Calcite that in-fills crustiform texture quartz presented in Fig. 7 has a small range in $\delta^{18}O_{Cc}$ values from 20.3 to 22.1‰ (Fig. 7c, d). The calcite does appear to have local zones of varied CL brightness, however there is no distinguishable relationship between areas of variable brightness and the measured $\delta^{18}O_{Cc}$ (Fig. 7c, d). Calcite that in-fills dolomite has a larger range, and slightly higher $\delta^{18}O_{Cc}$. Within the range of measured calcite that in-fills dolomite, the lowest $\delta^{18}O_{Cc}$ measurements are found in areas which show compositional zoning in CL immediately adjacent to zone 4 dolomite.

Calcite is observed in a separate setting where it has in-filled void space created by the alteration of pyrrhotite to pyrite. Distinctively, primary pyrite growth in these areas remains intact (Fig. 9a). Pyrite which formed by alteration of pyrrhotite has a patchy or mottled intergrowth texture with calcite, and areas filled with late calcite have outlines consistent with anhedral pyrrhotite growth in separate, less-altered samples (Fig. 9a). Cathodoluminescence images of the calcite in these replacement areas shows a mottled growth pattern which is not recognizable in back scattered electron images (Fig. 9b, c). Measurements of the variable mottled textures consistently produce high $\delta^{18}O_{Cc}$ values with a wide range (20.5 to 29.3‰), and gradients up to 9‰/50 μm. There does not appear to be any consistent recognizable correlation of CL, $\delta^{18}O_{Cc}$ and the Ca, Mg, Fe and Mn compositions.

A < 100 μm wide calcite microveinlet (Fig. 10) cross-cutting quartz in sample EH1505, is so small it was only identified by effervescence upon application of HCl on a primary quartz vein hand sample. Zoning in the microveinlet observed in backscattered electron images is related to Fe concentration, with up to 2.5 wt% FeO in a 15–20 μm band. Along the closely examined length of the fracture, the Fe-rich brighter (BSE) band is observed on alternating veinlet selvages locally. A distinctive bright CL band (< 5 μm wide) is observed mostly between the Fe-rich zone and the Fe-poor calcite, but also outside both zones along the veinlet selvage (Fig. 10i). Because of its size, the $\delta^{18}O_{Cc}$ or Ca, Fe, Mg, Mn composition of this bright CL band is not easily measurable, but appears to be intermediate brightness in BSE, therefore intermediate in

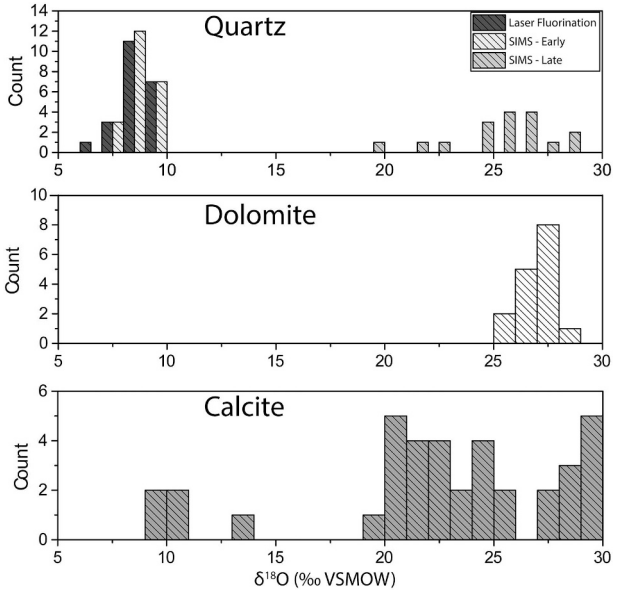

Fig. 6. Histograms of $\delta^{18}O$ (‰ VSMOW) values measured in quartz, dolomite and calcite. Small legend refers to quartz only. SIMS – Early = values measured in primary mineralized vein zone quartz, SIMS – Late = values measured in late crustiform textured quartz-carbonate veinlet.

Fe composition (0 to 2.5 wt% FeO). As well, the bright CL suggests it may contain Mn. *In situ* SIMS analyses of the calcite show a bi-modal population of low (9.6 to 13.3‰), and high (20.0 to 24.4‰) $\delta^{18}O_{Cc}$ values (Fig. 10).

5. Discussion

5.1. Chronology of veins, mineralization and metamorphism

From these results along with previous works, we interpret four important hydrothermal or metamorphic events, two of which contain direct evidence for gold mineralization/remobilization, and the other two being more speculative. The initial mineralization formed in the root zones of a VMS system. Quartz veins mineralized with pyrite and chalcopyrite were emplaced along with gold (Haroldson et al., 2018a) (Fig. 3a, b). After formation, the deposit was subjected to amphibolite grade regional metamorphism which likely remobilized gold (Haroldson et al., 2018b). Still later, alteration of the deposit (primarily the conversion of pyrite to pyrrhotite) occurred from reduced fluids circulated by emplacement of the nearby Wolf River Batholith (Haroldson et al., 2018b). Lastly, MVT fluids that circulated in the deposit are linked with gold mineralization/remobilization, along with the emplacement of various telluride phases and copper mineralization (Haroldson et al., 2018a, 2018b). The late MVT fluids emplaced numerous quartz and carbonate gangue phases (Fig. 3c, d) which are the subject of discussion in Section 5.3.

5.2. Primary mineralization

Measured $\delta^{18}O_{Qtz}$ of bulk quartz from the Reef Deposit plotted according to individual mineralized vein zones shows a distinct spatial trend (Fig. 5). The lowest $\delta^{18}O_{Qtz}$ values are found in the northwestern most vein zone and zones have increasingly higher $\delta^{18}O_{Qtz}$ towards the southeast (Figs. 2 and 5). The systematic spatial nature of the observed variation suggests the measured values are of primary hydrothermal quartz (Fig. 5). Resetting during subsequent regional deformation would have homogenized the $\delta^{18}O_{Qtz}$ values. Hydrothermal alteration during emplacement of the nearby Wolf River Batholith would have been hottest to the SE and created the opposite spatial pattern.

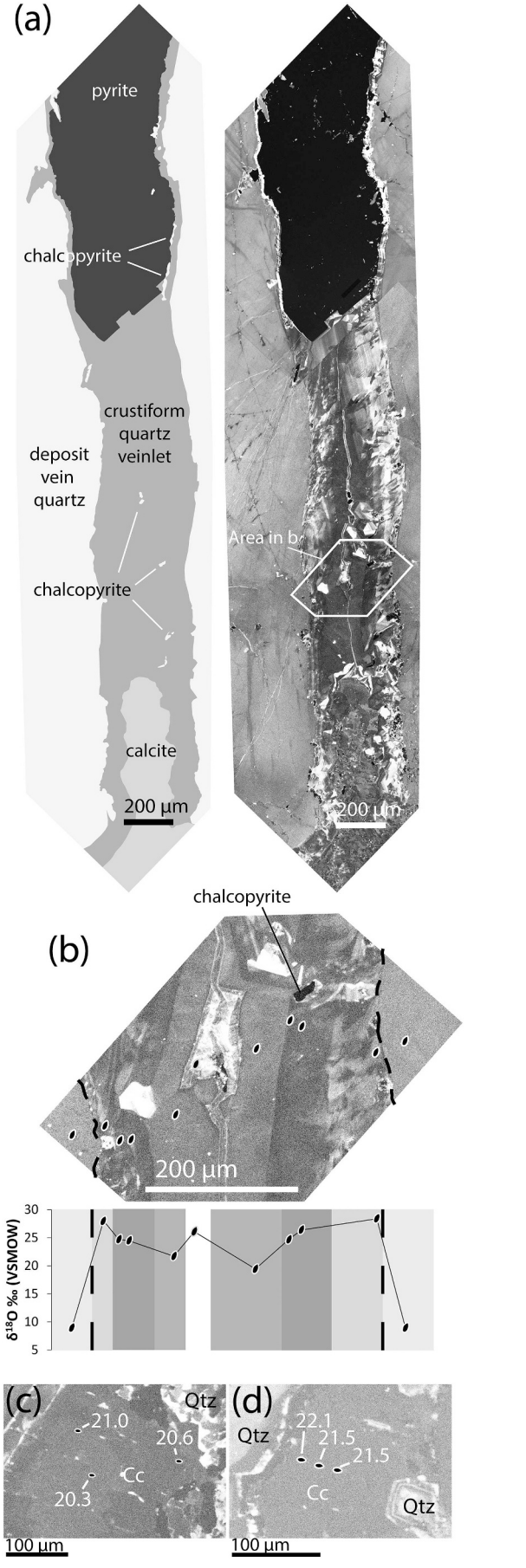

(caption on next page)

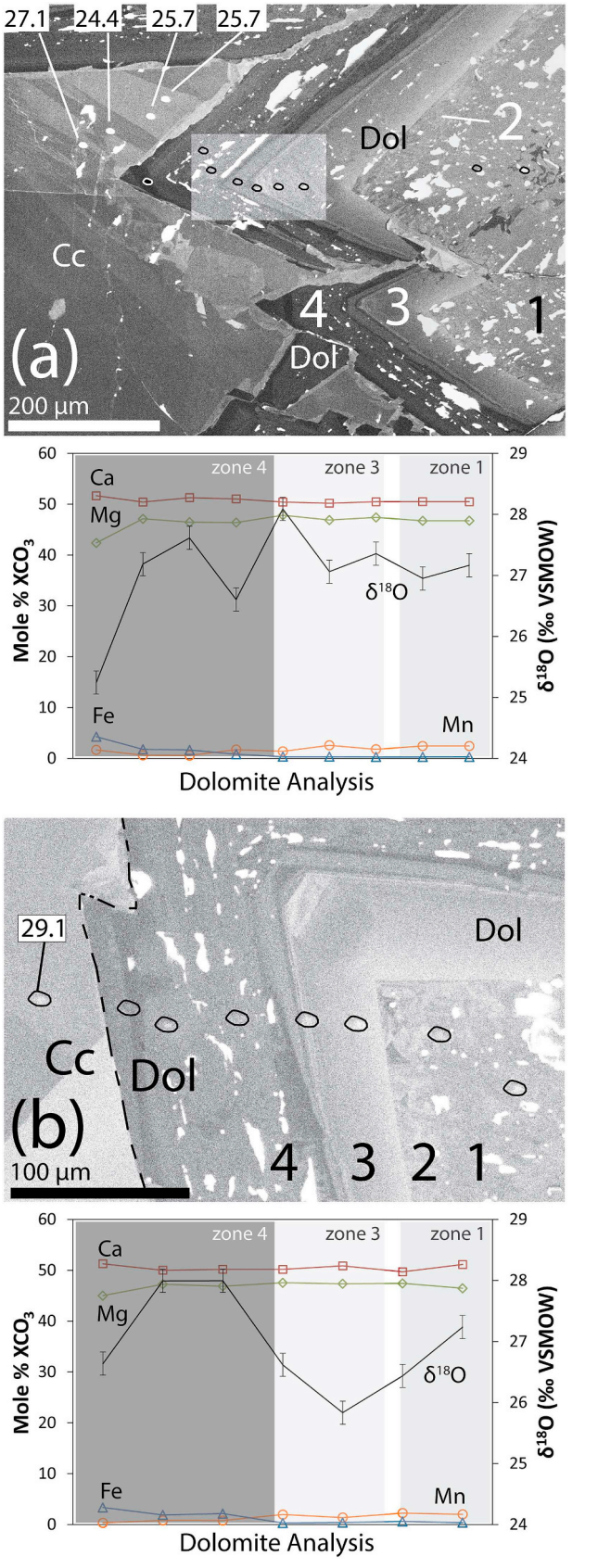

Fig. 7. Oxygen isotope measurement of a crustiform quartz and calcite veinlet, cross-cutting primary mineralized vein zone quartz in sample EH1509. (a) Schematic representation (left) and actual cathodoluminescence image (right) of veinlet showing pyrite, chalcopyrite coincident with crustiform quartz, and later calcite mineralization. (b) Inset of area identified in (a) with highlighted SIMS analysis pits and measured $\delta^{18}O_{Qtz}$ values plotted directly below the image. Data points at each end of the transect were measured in bounding quartz. (c–d) Cathodoluminescence images of areas containing calcite, from separate sample mount (RC01), but same veinlet identified in (a) with SIMS analyses pits highlighted by measured $\delta^{18}O_{Cc}$.

Laser fluorination $\delta^{18}O_{Qtz}$ values across individual vein zones have no spatial correlation horizontally or vertically. Assuming no variation of $\delta^{18}O_{H2O}$ for the hydrothermal fluid which formed the vein zones, the northwestern vein zone formed at the highest temperature. Temperature variation amongst zones could indicate the individual vein zones formed sequentially during a steady increase or decrease in temperature. A second interpretation would be the vein zones formed synchronously, within a thermal gradient outward from the heat source, which would have been located northwest of the current deposit location and orientation. Yet another interpretation is a variation in $\delta^{18}O_{H2O}$ due to differing amounts of water rock interaction.

The value of $\delta^{18}O_{H2O}$ for VMS deposits is usually estimated to be within a small range of seawater at the time of formation, and $\delta^{18}O_{H2O}$ values $> \sim -1$‰ have been used to argue for the involvement of magmatic sourced fluids (de Ronde, 1995). The temperature range in the hydrothermal setting underlying a VMS deposit is typically 300 to 400 °C (Franklin et al., 2005). Plotting the range of measured $\delta^{18}O_{Qtz}$ values on isopleths of $\delta^{18}O_{Qtz}$ in a plot of temperature *vs.* starting $\delta^{18}O_{H2O}$ and capping the expected temperature range to be < 400 °C, we find the likely range of $\delta^{18}O_{H2O}$ to be ≤2.6‰ (Fig. 11). The average $\delta^{18}O_{H2O}$ of seawater is proposed to have been as low as −8‰ during the Penokean orogeny (Jaffrés et al., 2007), while others have argued for a value similar to a modern ice-free world (−1‰) (Holmden and Muehlenbachs, 1993). In either case, the measured $\delta^{18}O_{Qtz}$ values consistent with precipitation from $\delta^{18}O_{H2O}$ of ≤2.6‰ (Fig. 11), may have been elevated above the likely seawater $\delta^{18}O_{H2O}$ value at the time of formation. The shift from negative $\delta^{18}O_{H2O}$ values to possibly 2.6‰ may have involved magmatic fluid, or may represent wallrock interaction or a combination of both.

No correlation is observed with primary $\delta^{18}O_{Qtz}$ and the gold grades or with copper grades (Fig. 12). Assayed sample intervals are typically ~1 m in length, and therefore a large amount of variation is possible within an individual zone, both in gold grade, and $\delta^{18}O_{Qtz}$ due to a 'nugget' distribution effect. It is likely that distribution of these ore metals has been overprinted by later mineralization/remobilization and this has masked any original correlation between $\delta^{18}O_{Qtz}$ and mineralization.

5.3. Secondary gangue mineralization

The presence of high $\delta^{18}O$ (19 to 30‰) quartz, calcite and dolomite in late textural settings, is observed by *in situ* SIMS measurements. We first discuss the potential secondary fluid sources responsible for the secondary mineralization in Section 5.3.1. We then discuss 5 individual analytical settings (quartz, dolomite and 3 calcite settings in Sections 5.3.2 to 5.3.6). A complex history of gangue mineralization is interpreted to involve multiple fluids with variable temperatures.

5.3.1. Potential secondary fluid sources

A summary of possible fluid sources for high $\delta^{18}O$ gangue minerals measured *in situ* in the Reef Deposit is given in Table 3. The geologic history of the region is poorly constrained due to a lack of exposure in the area. What is known of the history is complex and involves multiple magmatic and deformational events within a 200 km radius of the Reef Deposit.

(caption on next page)

Fig. 8. Measurement of dolomite and calcite in sample EH1512 by SIMS and EPMA. (a) Dolomite growth zones (1–4) discussed in the text are identified. SIMS pits in dolomite and respective EPMA analyses are plotted below the image corresponding with pits located from left to right. Ca, Mg, Fe and Mn error are within size of data point, $\delta^{18}O$ are 2SD. Measured $\delta^{18}O_{Cc}$ of four calcite SIMS pits are annotated in the image. (b) Same description as for (a), with one $\delta^{18}O_{Cc}$ SIMS pit value annotated.

There are multiple post-Penokean magmatic events in the region. A widespread post-orogenic granitic suite formed at 1760 Ma (Sims et al., 1989). Mesoproterozoic anorogenic magmatism occurred in two distinct episodes locally. The first episode emplaced the Wausau syenite and the Nine Mile granite of the Wausau syenite complex (1522 Ma and 1506 Ma, respectively), which are located within 20 km west of the Reef Deposit (Dewane and Van Schmus, 2007). The second episode emplaced the Wolf River Batholith over the time interval 1484–1468 Ma directly adjacent and east of the deposit (Dewane and Van Schmus, 2007). Post-Silurian ultramafic igneous activity is reported in Kenosha County, ~200 km SE of the Reef Deposit (Carlson and Adams, 1997). Jurassic kimberlites are identified ~180 km NE of the Reef Deposit in Upper Peninsula Michigan (Cannon and Mudrey, 1981; Zartman et al., 2013). Common magmatic (mafic to felsic) $\delta^{18}O_{H2O}$ values are in the +5.5 to +10‰ range for ore deposit systems, and we would expect ultramafic igneous activity closer to a primary mantle value of +5.5‰ (Taylor, 1979).

The Yavapai province accreted to the south of the Marshfield and Pembine-Wausau terranes along the Spirit Lake tectonic zone *ca.* 1.7 Ga, and the Mazatzal orogeny accreted the Mazatzal province to the south of the Yavapai province ca 1.6 Ga (Whitmeyer and Karlstrom, 2007). Metamorphic fluids associated with the Yavapai or Mazatzal orogenies would likely fall in the commonly accepted range in $\delta^{18}O$ from +3 to +20‰ (Sheppard, 1986).

Mississippi Valley-type fluids have been recognized to form a late gold mineralization/remobilization event in the Reef Deposit (Haroldson et al., 2018a, 2018b). Timing and source of the late MVT fluid remains ambiguous with competing models invoking Devonian to Permian fluids from one of three sources. The first source is from sedimentary basinal brine fluid circulated by gravity driven flow. Basinal brines have been estimated to have $\delta^{18}O_{H2O}$ compositions between −3‰ and +2‰, with increase in $\delta^{18}O_{H2O}$ due to water/rock interactions along the flow path (Wilkinson et al., 1992; Kesler et al., 1997; Pollington et al., 2011; Hyodo et al., 2014; Śliwiński et al., 2016b; Pollington et al., 2016). The second fluid source is local meteoric water (Haroldson et al., 2018b). During the Permian, the region was located near the equator, and rainwater forming the local meteoric water would have a $\delta^{18}O_{H2O}$ value approximating the average value of early Paleozoic seawater (−5‰ to −1‰; *e.g.*, Holmden and Muehlenbachs, 1993; Came et al., 2007; Jaffrés et al., 2007). The third source of fluid involves the circulation of shield brines, deep groundwater circulating in crystalline basement rocks, by high heat-producing (anomalously radiogenic) granites of the Wolf River Batholith (Spirakis and Heyl, 1996; Haroldson et al., 2018b). Measured $\delta^{18}O$ of shield brines in the Archean Canadian Shield range from −10 to −20‰ and a possible source brine has been modelled to have $\delta^{18}O_{H2O}$ compositions ranging from −7 to −10‰ (Frape and Fritz, 1987; Bottomley et al., 1999).

5.3.2. Quartz

The zonation from high $\delta^{18}O_{Qtz}$ in the crustiform vein margins to lower $\delta^{18}O_{Qtz}$ in the center (Fig. 7b) likely reflects a gradual increase in temperature from the earliest outer growth quartz to subsequent growth bands. A return to more moderate temperatures may be indicated by one SIMS analysis of a brighter CL zone in the center of the veinlet.

Crustiform quartz growth temperatures estimated from possible oxygen isotope compositions of the various fluid sources discussed in

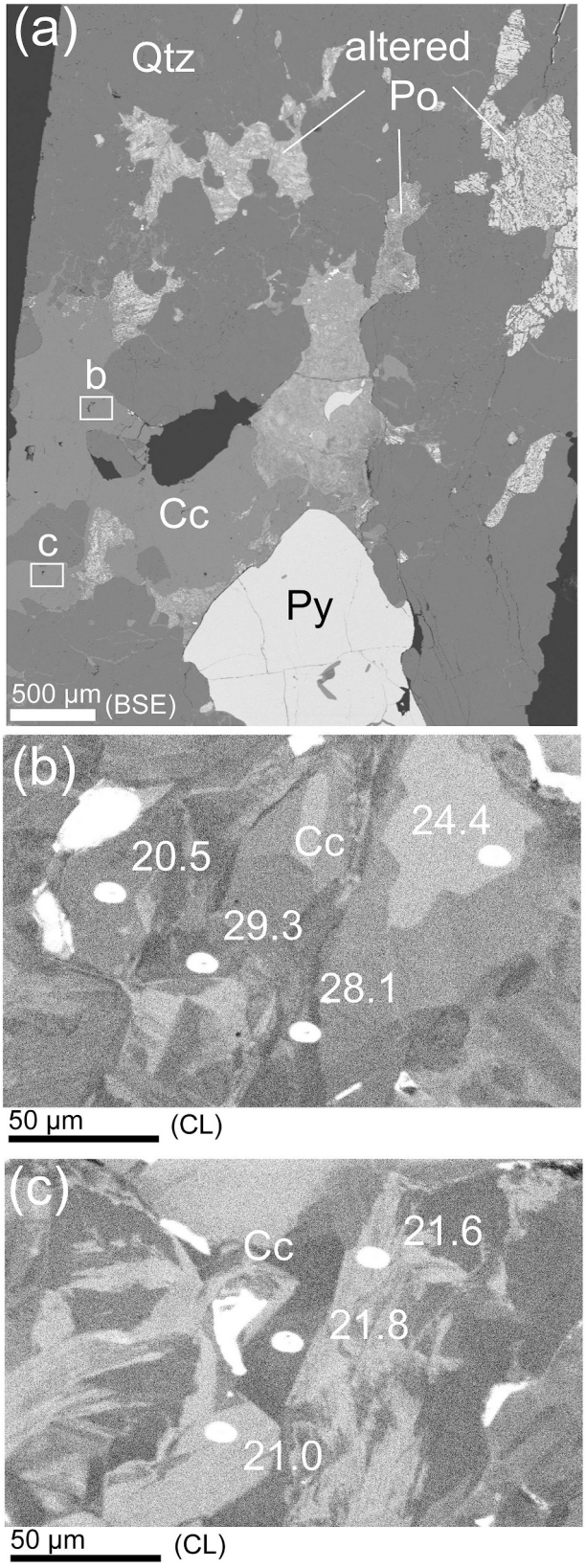

Fig. 9. Back Scattered Electron (BSE) and Cathodoluminescence (CL) images of sample EH1530 showing SIMS analysis of calcite observed replacing pyrrhotite. (a) BSE image showing alteration textures. Note that pyrrhotite has altered to patchy texture pyrite, whereas primary pyrite remains unaltered. Location of insets (b) and (c) are identified in (a). (b) CL image of area identified in (a) with SIMS analysis pits and measured $\delta^{18}O_{Cc}$ values (‰ VSMOW). (c) Similar to (b). Qtz – quartz, Po – pyrrhotite, Cc – calcite, Py – pyrite.

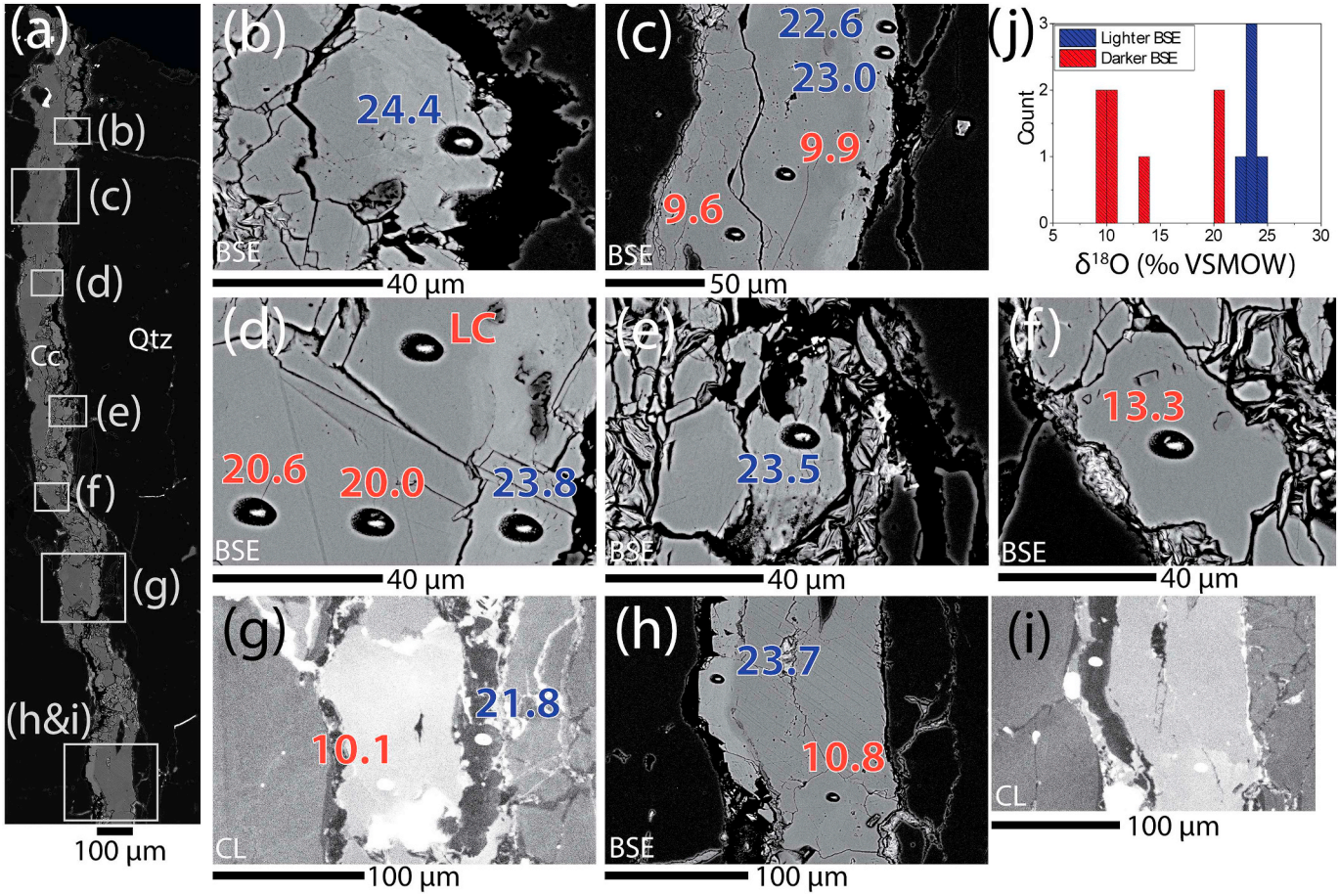

Fig. 10. Back scattered electron and cathodoluminescence images of a calcite microveinlet in sample EH1505. (a) BSE image of ~100 µm wide calcite microfracture hosted in quartz. Figures (b)–(i) are inset images identified in image (a), with image type identified in lower left corner (BSE – Back scattered electron, CL – Cathodoluminescence). In insets (b)–(h), measured $\delta^{18}O_{Cc}$ values of SIMS pits are given, with red values for pits located in darker BSE calcite, and blue values for pits located in lighter BSE calcite. The BSE intensity is related to Fe content, with the brighter BSE calcite having higher Fe content. The histogram shows the overall distribution of measured $\delta^{18}O_{Cc}$ values. (i) Cathodoluminescence image of inset (h), notice the brightest CL calcite is located to the left of the dark CL calcite band. LC - low counts (SIMS analysis). (For interpretation of the references to colour in this figure legend, the reader is referred to the web version of this article.)

Section 5.3.1 are plotted in Fig. 13. Fluids originally from a magmatic or metamorphic source ($\delta^{18}O > 3$) would have a temperature minimum of 75 °C for the highest $\delta^{18}O_{Qtz}$ value (28.4‰) and 140 °C for the lowest $\delta^{18}O_{Qtz}$ value (19.4‰). These temperatures are relatively low for a magmatic or metamorphic fluid, requiring a distal derivation. Methane-bearing fluid inclusions associated with the Wolf River Batholith event indicate fluid temperatures as high as 700 °C (Haroldson et al., 2018b). However, it is reasonable to assume a protracted history of the Wolf River Batholith emplacement, with the higher temperature being derived from nearby magmatic activity, and the lower temperature fluid derived from lower portions or some other, more distal portion of the batholith, or during a later stage as the contact cooled. Using the upper estimate for magmatic water of 10‰ gives a range from 120 to 240 °C, which is somewhat more reasonable for a magmatic fluid, however still needing a distal derivation. Even heavier $\delta^{18}O_{H2O}$ values (> 10‰) would be associated with a metamorphic fluid and temperature calculations could range from temperatures commonly observed for metamorphic fluids to temperatures exceeding those observed in mafic igneous melts. We are unable to rule out a distal magmatic or a metamorphic fluid for the late crustiform quartz veinlets.

As discussed in Section 5.3.1, there are multiple possibilities for a starting $\delta^{18}O_{H2O}$ related to the MVT fluid. Temperature estimates from these values range from 18 to > 300 °C (Fig. 13). The shield brine temperature estimates are too low. Meteoric water would be low salinity and therefore not capable of copper transport as copper is typically transported in a chloride complex, especially at low temperature (Brugger et al., 2007; Sherman, 2007). If the MVT fluids are not shield brines or meteoric water, then the minimum temperature would be ~50 °C (Fig. 13).

To evaluate the potential of an MVT fluid being responsible for precipitation of quartz, we compare with a recent study of quartz overgrowths in the Mt. Simon Formation, which is the basal sandstone unit of the overlying Paleozoic sedimentary sequence (Pollington et al., 2016). Samples in the Pollington et al. (2016) study were collected within a few meters of the Precambrian unconformity from outcrops ~50 km south of the Reef Deposit (Fig. 1). Mt. Simon formation quartz overgrowths record two distinct events, near-surface temperature diagenetic growth is interpreted from overgrowths averaging $\delta^{18}O$ ~30.6 ± 2.9‰, and growth from warmer fluid is interpreted from a separate sample at a nearby outcrop with $\delta^{18}O_{Qtz}$ values 2 to 12‰ lower. These lower values are bracketed by higher $\delta^{18}O_{Qtz}$ values measured towards the edges of quartz overgrowths, suggesting the warmer hydrothermal fluid as a short-lived event. In the Reef Deposit crustiform quartz veinlets, $\delta^{18}O_{Qtz}$ values range from of 19.4 to 28.4‰, consistent with growth in the warmer fluid observed in Pollington et al. (2016). There is also a systematic decrease in $\delta^{18}O_{Qtz}$ for subsequent growth bands observed, possibly indicating an increase in temperature during each subsequent growth. As well, higher $\delta^{18}O_{Qtz}$ of 26.1‰ in the youngest quartz measured may indicate a return towards relatively cooler temperature growth (Fig. 7).

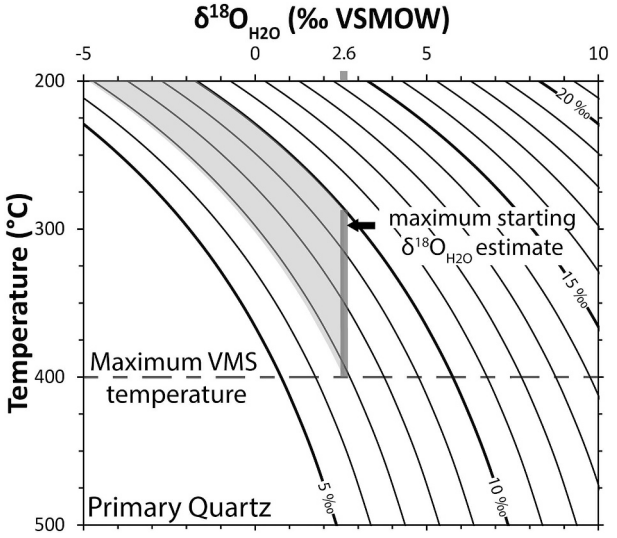

Fig. 11. Temperature *vs.* $\delta^{18}O_{H2O}$ for measured $\delta^{18}O_{Qtz}$ values with isopleths of $\delta^{18}O_{Qtz}$ (Sharp et al., 2016). The range of $\delta^{18}O_{Qtz}$ values measured are highlighted in grey. The intersection of a maximum temperature (400 °C) with all $\delta^{18}O_{Qtz}$ values measured corresponds with a starting $\delta^{18}O_{H2O}$ of 2.6‰, assuming a constant $\delta^{18}O_{H2O}$. The elevation above a seawater estimate of −1‰ could be due to involvement of magmatic fluid, however it could also simply represent uncertainty in the seawater estimate for the Paleoproterozoic.

Pollington et al. (2016) use an estimate for the starting $\delta^{18}O_{H2O}$ of −3‰ (approximate early Paleozoic seawater), corresponding to a temperature range of ~45 to 120 °C for precipitation of quartz overgrowths. Using the same estimate of −3‰ for a starting $\delta^{18}O_{H2O}$ corresponds to temperatures between ~45 to 90 °C for the crustiform quartz in the Reef Deposit, within the temperature range observed for the Mt. Simon overgrowths. Thus the hydrothermal fluid event documented by Pollington et al. (2016), supports the occurrence of Paleozoic fluid movement in central Wisconsin.

5.3.3. Dolomite

Dolomite growth temperatures estimated for a range of possible oxygen isotope compositions of the various MVT fluid sources discussed in Section 5.3.1 are plotted in Fig. 14. Within zone 4 the outermost $\delta^{18}O_{Dol}$ measurement is consistently lower, suggesting an increase in temperature during zone 4 growth. However, there is little variation in the $\delta^{18}O_{Dol}$ measured in the dolomite (~25 to 28‰) across all zones, suggesting little temperature variation associated with the zonation seen by CL.

5.3.4. Calcite that in-fills late quartz and dolomite

Calcite (that in-fills quartz and dolomite) temperatures estimated for the range of possible oxygen isotope compositions of the various fluid sources discussed in Section 5.3.1, are plotted in Fig. 15. Calcite, that in-filled after dolomite, hosts secondary fluid inclusions with estimated formation temperatures ranging from < 50 to 103 °C (Haroldson et al., 2018b). The same calcite has measured $\delta^{18}O_{Cc}$ values ranging from 24.2 to 29.3‰. Using a starting $\delta^{18}O_{H2O}$ of −5 to +2‰ to include both, the basinal brine and the meteoric water models, leads to temperature estimates of 46 to 115 °C (Fig. 15). The similarity in measured fluid inclusion temperatures and estimated oxygen isotope temperatures is striking, however because the fluid inclusions are secondary, a direct genetic relationship is not observed. It does appear that a similar temperature range was observed for the fluid initially forming the calcite and later healing of small fractures in the calcite.

5.3.5. Calcite replacing pyrrhotite

Importantly, the calcite in this setting is texturally associated with

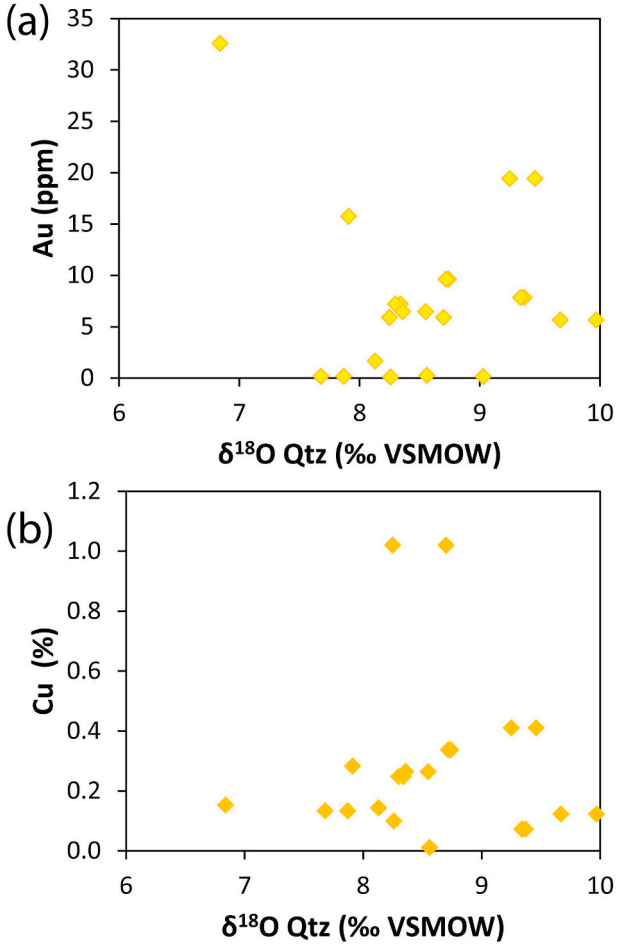

Fig. 12. $\delta^{18}O$ measured in quartz separates from primary mineralized veins *vs.* assay grade. No correlation is seen between the oxygen isotope values and assay values. (a) gold in ppm *vs.* $\delta^{18}O_{Qtz}$. (b) Copper in percent abundance *vs.* $\delta^{18}O_{Qtz}$. Assay values represent ~1 m drill core segments and $\delta^{18}O_{Qtz}$ measurements are matched with the interval from which they were selected. Assay values are provided from Aquila Resources Inc.

altaite (PbTe) in mineral clusters of Au and telluride minerals measured for Pb isotope compositions which were found to be radiogenic and therefore relatively young, and thus are associated with the late overprinting mineralization (Haroldson et al., 2018a). This does not mean that the overprinting mineralization is only evident in places with pyrrhotite destructive alteration. As is evidenced by Pb isotopes and fluid inclusions, the late overprinting fluid is observed throughout the deposit, including areas where calcite replacement of pyrrhotite is not evident.

Calcite replacing pyrrhotite has a range in $\delta^{18}O_{Cc}$ values (20.5 to 29.3‰) which includes the range measured in calcite in Section 5.3.4 and extends to lower $\delta^{18}O_{Cc}$. This is consistent with similar temperatures of precipitation as well as an extension to higher temperatures approaching 150 °C (using starting $\delta^{18}O_{H2O}$ values of −5 to +2‰) (Fig. 16). These observations are consistent with low and variable temperatures and fluid compositions associated with late fluid infiltration.

5.3.6. Calcite microveinlets

Calcite microveinlet temperatures estimated for the possible oxygen isotope compositions of the various fluid sources discussed in Section 5.3.1 are plotted in Fig. 17. Of particular interest, are the relatively low $\delta^{18}O_{Cc}$ values (9.6 to 13.3‰). As discussed in Section 5.3.1, the calcite would have formed post regional deformation. To explain the low

Table 3
Oxygen isotope compositions of potential fluid source reservoirs.

Geologic event	Age	Age Reference	$\delta^{18}O_{H2O}$ (‰ VSMOW)	Reference
Regional metamorphism	1845 to 1833 Ma	Schulz and Cannon, 2007	+3 to +20	Sheppard, 1986
Yavapai and Mazatzal metamorphic fluid	~1750 to 1650 Ma	Whitmeyer and Karlstrom, 2007	+3 to +20	Sheppard, 1986
Wolf River Batholith (anorogenic magmatism)	1522 to 1468 Ma	Dewane and Van Schmus, 2007	+5.5 to 10	Taylor, 1979 (magmatic values)
Mid-continent rift	~1100 Ma	Van Schmus and Hinze, 1985	+5.5 to 10	Taylor, 1979 (magmatic values)
Kimberlite magmatism	< 420 Ma	Carlson and Adams, 1997	+5.5 to 10	Taylor, 1979 (magmatic values)
Basinal brine	~270 Ma	Brannon et al., 1992	−3 to +2	Pollington et al., 2016 (and references within)
High heat-producing granite - meteoric water	~270 Ma	Brannon et al., 1992	−5 to −1	Holmden and Muehlenbachs, 1993; Came et al., 2007; Jaffrés et al., 2007
High heat-producing granite - shield brine	~270 Ma	Brannon et al., 1992	−10 to −7	Frape and Fritz, 1987 and Bottomley et al., 1999

$\delta^{18}O_{Cc}$ values, one could assume a metamorphic or a magmatic source with formation temperatures ≥320 °C. This temperature range would likely require relatively proximal derivation. Calcite formed at lower temperatures (< 210 °C) would require an even lower starting $\delta^{18}O_{H2O}$ such as meteoric water or the postulated shield brine fluid.

There is a section of this microveinlet where high $\delta^{18}O_{Cc}$ values were measured in the low-Fe calcite evident in SIMS analyses (Fig. 10d). Volume diffusion of O into calcite will not be important at these low temperatures. It is not clear why the high $\delta^{18}O_{Cc}$ values exist locally in the low-Fe calcite. The high $\delta^{18}O_{Cc}$ values are likely formed from a late, low-temperature fluid, similar to fluids described in the previous secondary mineralization settings. In this case it would have been a relatively Fe-deficient fluid.

5.4. Mississippi valley-type mineralization

The petrogenetic positioning of chalcopyrite mineralization, post-dating the growth of late dolomite and preceding the growth of void-filling calcite, in late carbonate veinlets of the Reef Deposit bears a striking resemblance to chalcopyrite mineralization depicted for MVT deposits of the Viburnum trend, (Voss et al., 1989). Using a combination of reflected light spectroscopy of Viburnum trend MVT deposit sulfides as well as transmitted light and CL imaging of carbonate minerals, Voss et al. (1989) identified that specific sulfide minerals accompanied various stages of carbonate growth. Similar CL patterns, growth textures, and trace element compositions are also found in dolomite cements across southeast Missouri (Cathles, 1993). Because of the substantial distance between southeast Missouri and the Reef Deposit in northern Wisconsin, direct correlation of the fluid evolution is not possible (Searl, 1988). However, MVT fluids at the Reef Deposit could be sourced from the Illinois Basin and a similar sequence of individual pulses of regional fluid flow might be controlled by changes in the large scale tectonic forces. The CL patterns, trace element compositions and oxygen isotope ratios of dolomite in the Reef Deposit and Viburnum Trend are similar to carbonate cement growth histories in sedimentary formations studied in northern Illinois as well as sedimentary formations hosting mineralization in the Upper Mississippi Valley (UMV) district of SW Wisconsin (Smith and Simo, 1997; Śliwiński et al., 2016b). The growth typically displays four dolomite growth zones visible in CL (Fig. 4), with some loss due to intermittent dissolution, most commonly the dissolution of the second zone. The third CL zone is typically the brightest in CL, followed by a final fourth growth zone with low CL attributed to an increase in Fe (Voss et al., 1989; Smith and Simo, 1997; Śliwiński et al., 2016b). When measured by SIMS, the $\delta^{18}O_{Dol}$ of dolomite growth zones are interpreted, at least in part, as formed from MVT fluids (Śliwiński et al., 2016b). Repeated observations of similar carbonate growth possibly related to MVT fluid flow seems to bridge the distance between southern Missouri and northern Wisconsin (Fig. 18). Indeed, extensive MVT fluid movement across the region, during the Paleozoic (perhaps multiple episodes) has been identified by multiple workers (Liu et al., 2003; Luczaj, 2006; Craddock et al., 2017).

Chalcopyrite mineralization is common in VMS deposits, but is also observed in UMV district and other MVT deposits (Heyl et al., 1959; Kutz and Spry, 1989; Voss et al., 1989, Leach et al., 2010). The presence of chalcopyrite in the crustiform quartz veinlet found at various growth surfaces is in keeping with the MVT fluid model. Chalcopyrite appears to have formed immediately preceding or during the highest temperature quartz mineralization in late quartz veinlets. As well, the highest temperatures in dolomite (Section 5.3.3) are inferred in a zone immediately preceding chalcopyrite mineralization. A decrease in temperatures is then suggested in the subsequent calcite growth formed after this chalcopyrite. This may indicate a higher temperature fluid during chalcopyrite growth, although inconsistent with inverse carbonate dissolution. Furthermore, there appears to be dolomite dissolution consistent with this higher temperature event suggesting a lower pH. As

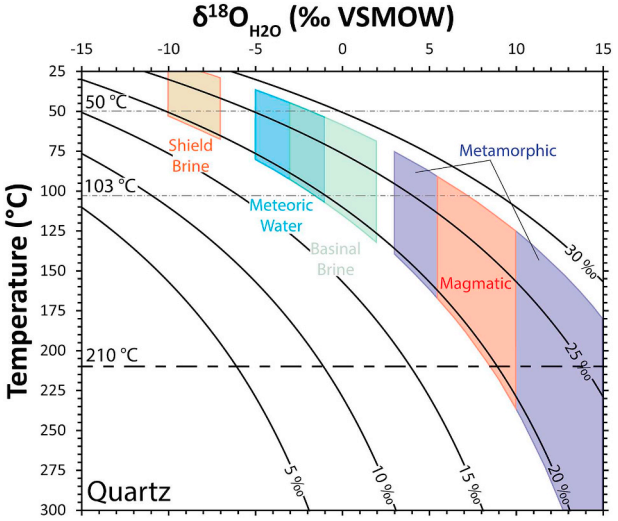

Fig. 13. Temperature *vs.* $\delta^{18}O_{H2O}$ with isopleths for $\delta^{18}O_{Qtz}$ in equilibrium. Measured values for high $\delta^{18}O_{Qtz}$ from Fig. 7 (19.4 to 28.4‰). The range of $\delta^{18}O_{Qtz}$ values measured are highlighted where corresponding to various $\delta^{18}O_{H2O}$ values discussed in Section 5.3.1. Dashed lines at 50, 103 and 210 °C represent fluid inclusion temperatures associated with the late low temperature fluid system (Haroldson et al., 2018b).

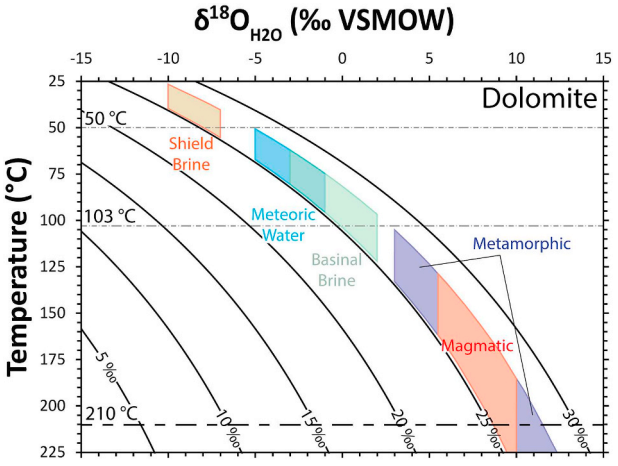

Fig. 14. Temperature *vs.* $\delta^{18}O_{H2O}$ with isopleths for $\delta^{18}O_{Dol}$ in equilibrium. Measured $\delta^{18}O_{Dol}$ values from Fig. 8 (25.2 to 28.1‰) are highlighted where corresponding to various $\delta^{18}O_{H2O}$ values discussed in Section 5.3.1. Dashed lines at 50, 103 and 210 °C represent fluid inclusion temperatures associated with the late low temperature fluid system (Haroldson et al., 2018b). Dashed grey lines are from a calcite hosted fluid inclusion assemblage (FIA), dashed black is maximum temperatures obtained from quartz-hosted FIA.

well, a strong dissolution surface is observed after growth of zone 3 dolomite (Fig. 4) and a weak dissolution surface possibly observed after growth of zone 2, suggesting multiple infiltrations of a low pH fluid.

In all of the gangue mineralization (calcite, dolomite or quartz) that cross-cuts the initial vein quartz, a range of temperatures is inferred from the variable $\delta^{18}O$, however, assuming a starting $\delta^{18}O_{H2O}$ of −5 to +2‰ for all of the settings, temperature estimates are consistently in the range of < 50 to 103 °C, consistent with homogenization temperatures measured in secondary fluid inclusions in the late calcite that in-fills dolomite. There is only one setting (the calcite microveinlet, Fig. 10) in which *in situ* SIMS analysis of gangue mineralization identifies temperature of precipitation consistent with the highest quartz hosted secondary fluid inclusion temperatures (210 °C) interpreted to be associated with the MVT event by Haroldson et al., 2018b. The quartz and various calcite settings record some variation in

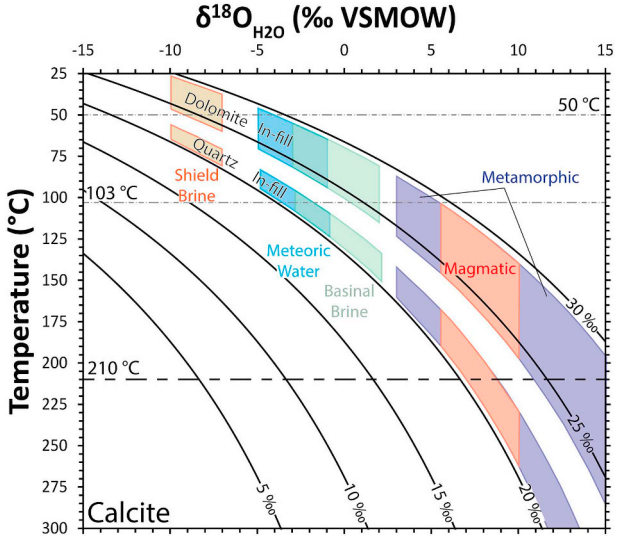

Fig. 15. Temperature *vs.* $\delta^{18}O_{H2O}$ with isopleths for $\delta^{18}O_{Cc}$ in equilibrium. Measured $\delta^{18}O_{Cc}$ values from Figs. 7 and 8 are highlighted where corresponding to various $\delta^{18}O_{H2O}$ values discussed in Section 5.3.1. The lower $\delta^{18}O_{Cc}$ (20.3 to 22.1‰) group is representative of calcite which in-fills quartz (Fig. 7), the higher $\delta^{18}O_{Cc}$ (24.2 to 29.3‰) group is representative of calcite which in-fills dolomite (Fig. 8). Dashed lines at 50, 103 and 210 °C represent fluid inclusion temperatures associated with the late low temperature fluid system (Haroldson et al., 2018b).

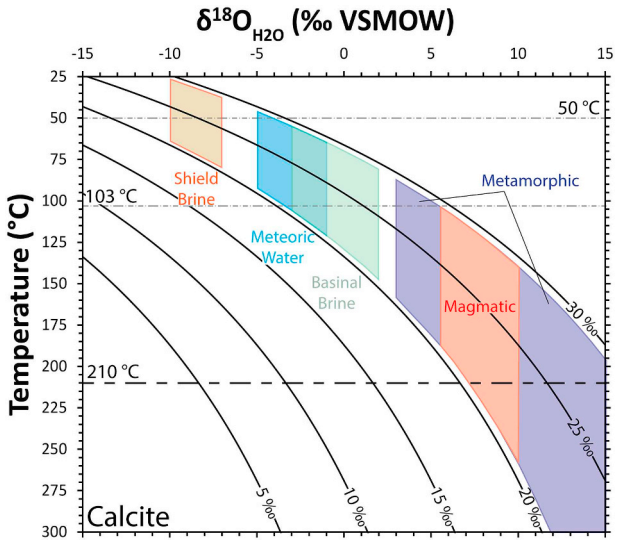

Fig. 16. Temperature *vs.* $\delta^{18}O_{H2O}$ with isopleths for $\delta^{18}O_{Cc}$ in equilibrium. Measured $\delta^{18}O_{Cc}$ values from Fig. 9 (20.5 to 29.3‰) are highlighted where corresponding to various $\delta^{18}O_{H2O}$ values discussed in Section 5.3.1. Dashed lines at 50, 103 and 210 °C represent fluid inclusion temperatures associated with the late low temperature fluid system (Haroldson et al., 2018b).

temperature; in particular the quartz shows increase in temperature in subsequent growth bands. The dolomite growth instead shows only small changes in $\delta^{18}O_{Dol}$, suggesting a small temperature gradient. The presence of dissolution surfaces in dolomite coincident with the mineralization of chalcopyrite is seen as evidence for the presence of a fluid that was not captured in the gangue mineral record.

Punctuated fluid events likely had a lower pH fluid responsible for carbonate dissolution, and the chalcopyrite mineralization may be evidence for the fluid to have been a relatively higher temperature. A mechanism to create these punctuated events would be local faulting during the Appalachian-Ouachita orogeny. Interacting with the

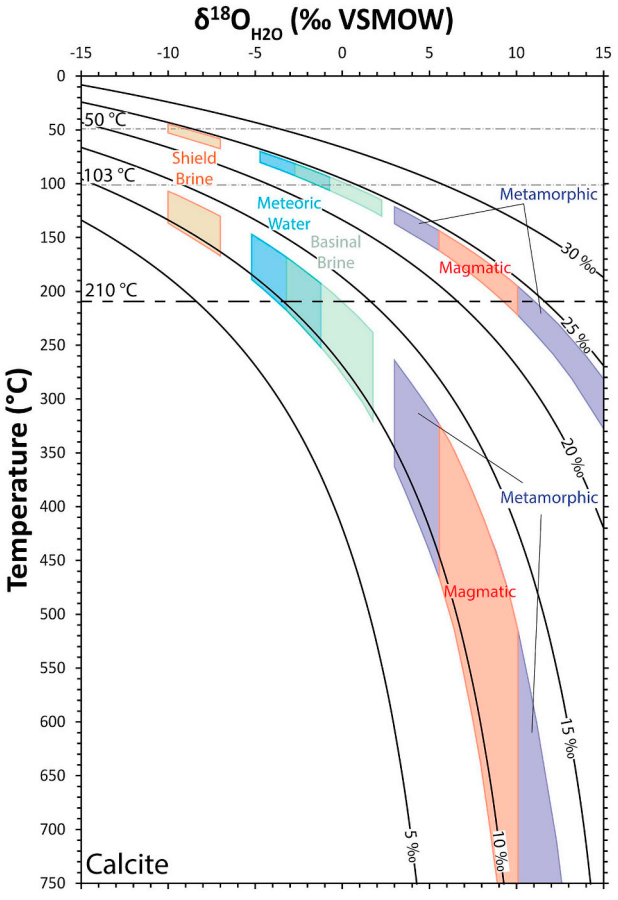

Fig. 17. Temperature *vs.* $\delta^{18}O_{H2O}$ with isopleths for $\delta^{18}O_{Cc}$ in equilibrium. Measured $\delta^{18}O_{Cc}$ values from Fig. 10 is highlighted where corresponding to various $\delta^{18}O_{H2O}$ values discussed in Section 5.3.1. Dashed lines at 50, 103 and 210 °C represent fluid inclusion temperatures associated with the late low temperature fluid system (Haroldson et al., 2018b).

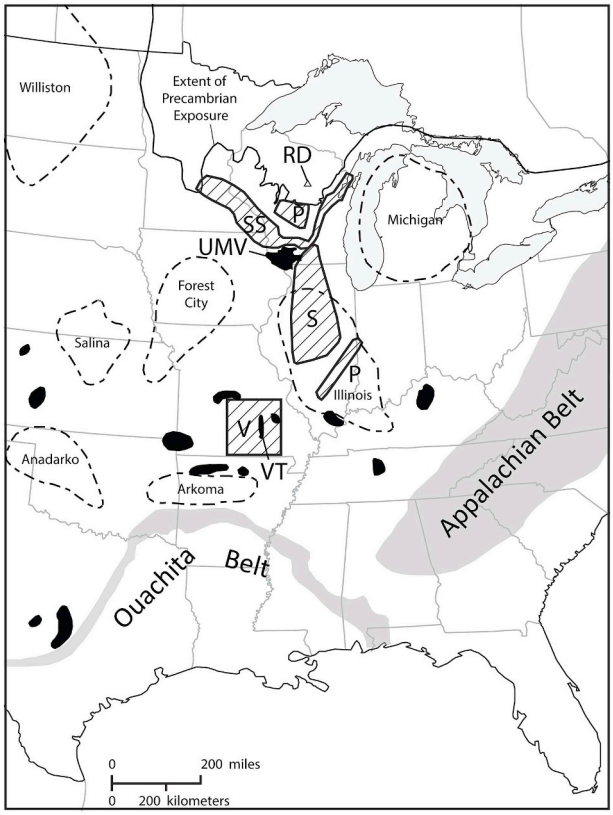

Fig. 18. Location of the Reef deposit relative to Mississippi Valley-type lead-zinc districts (black areas), major sedimentary basins (dashed outline) and tectonic belts (grey areas) after Oliver, 1986. RD = Reef Deposit, UMV = Upper Mississippi Valley district, VT = Viburnum Trend. Previous study areas discussed in the text are shown. V = Voss et al. (1989), SS = Smith and Simo (1997), S = Śliwiński et al. (2016b), P = Pollington et al. (2016).

crystalline basement *via* faulting would allow for a lower pH fluid, normally buffered by interaction with Paleozoic carbonate rocks. Furthermore, with enough time between these punctuated events, heat could have built up through radiogenic decay in local high heat-producing granites, as proposed by Spirakis and Heyl (1996). This suggests the late gangue mineralization (quartz, dolomite and calcite) formed during a steadier state growth from gravity driven fluids flowing through the cover sequence. The mineralization of Cu–Fe sulfides and Au-Ag-Pb tellurides were related to punctuated thermal events formed by fluids accessing deep sections of the nearby Wolf River Batholith along local faults that cut the basement.

6. Summary and conclusions

Oxygen isotope measurements of mineralized quartz veins by laser fluorination give $\delta^{18}O_{Qtz}$ values ranging from 6.8 to 10.0‰ suggesting that the Reef Deposit veins were initially formed by hydrothermally shifted seawater at temperatures of ~230 to 400 °C, consistent with the interpretation of a hydrothermal circulation system underlying a volcanogenic massive sulfide deposit. The oxygen isotope values of vein zones show a spatial correlation suggesting higher temperatures in the northwestern vein zones and lowest temperatures in the southeastern zones.

Secondary overprinting mineralization is recognized by *in situ* secondary ion mass spectrometry measurements giving high $\delta^{18}O$ ($\delta^{18}O$ > 19‰) measurements of quartz, dolomite and calcite in various textural settings. Small (10 μm to 0.5 cm) crustiform quartz veinlets show a progressive increase in temperature with a late return to relatively lower temperatures during growth. Carbonate veinlets (1–10 cm thick) have a typical paragenesis of 4 stages of dolomite growth and chalcopyrite growth was then followed by late calcite growth. High $\delta^{18}O_{Cc}$ is measured in late calcite, which in-filled both late quartz and late dolomite veinlets. High $\delta^{18}O_{Cc}$ is measured in late calcite observed replacing altered pyrrhotite. High $\delta^{18}O_{Cc}$ is also measured in banded calcite veinlets (~200 μm in size) formed alongside lower $\delta^{18}O$ calcite. The various high $\delta^{18}O$ gangue mineralization is found to be most consistent with low temperature growth, in most cases < 150 °C, which is also consistent with a late, low temperature system observed by past workers to be related to MVT mineralization.

Declaration of competing interest

The authors declare that they have no known competing financial interests or personal relationships that could have appeared to influence the work reported in this paper.

Acknowledgements

Michael Spicuzza assisted with laser fluorination analyses, Maciej Śliwiński assisted with SIMS calibrations and measurement corrections of carbonate, Aurélien Moy assisted with EPMA analyses and Brian Hess assisted with sample preparation. This research was supported by student research grants from the Society of Economic Geologists Canada Foundation and the Geological Society of America. This research was also supported by gifted research funds from Newmont Mining Inc. to the University of Wisconsin-Madison Department of Geoscience. EH

thanks Aquila Resources Inc. for access to samples. WiscSIMS is supported by NSF (EAR-1355590, -1658823) and UW-Madison. Comments from Bertrand Rottier, an anonymous reviewer and the editor helped to improve the manuscript.

Appendix A. Supplementary data

Supplementary data to this article can be found online at https://doi.org/10.1016/j.chemgeo.2019.119429.

References

Allan, M.A., Yardley, B.W.D., 2007. Tracking meteoric infiltration into a magmatic-hydrothermal system: a cathodoluminescence, oxygen isotope and trace element study of quartz from Mt. Leyshon, Australia. Chem. Geol. 240, 343–360. https://doi.org/10.1016/j.chemgeo.2007.03.004.

Anderson, J.L., 1983. In: Medaris Jr.L.G., Byers, C.W., Mickelson, D.M., Shanks, W.C. (Eds.), Proterozoic Anorogenic Granite Plutonism of North America, Proterozoic Geology: Selected Papers From an International Proterozoic Symposium. Geological Society of America Memoirs 161. pp. 133–154. https://doi.org/10.1130/MEM161-p133.

Bottomley, D.J., Katz, A., Chan, L.H., Starinsky, A., Douglas, M., Clark, I.D., Raven, K.G., 1999. The origin and evolution of Canadian Shield brines: evaporation or freezing of seawater? New lithium isotope and geochemical evidence from the Slave craton. Chemical Geology 155, 295–320. https://doi.org/10.1016/S0009-2541(98)00166-1.

Brannon, J.C., Podosek, F.A., McLimans, R.K., 1992. Alleghenian age of the Upper Mississippi Valley zinc-lead deposit determined by Rb-Sr dating of sphalerite. Nature 356, 509–511. https://doi.org/10.1038/356509a0.

Brugger, J., Etschmann, B., Liu, W., Testemale, D., Hazemann, J.L., Emerich, H., van Beek, W., Proux, O., 2007. An XAS study of the structure and thermodynamics of Cu (I) chloride complexes in brines up to high temperature (400 °C, 600 bar). Geochim. Cosmochim. Acta 71, 4920–4941. https://doi.org/10.1016/j.gca.2007.08.003.

Came, R.E., Eiler, J.M., Veizer, J., Azmy, K., Brand, U., Weidman, C.R., 2007. Coupling of surface temperatures and atmospheric CO_2 concentrations during the Paleozoic era. Nat. Lett. 449, 198–201. https://doi.org/10.1038/nature06085.

Cannon, W.F., Mudrey, M.G., 1981. The potential for diamond-bearing kimberlite in northern Michigan and Wisconsin. In: United States Geological Survey Circular 842, (15 p).

Carlson, S.M., Adams, G.W., 1997. The diamondiferous Six-pak ultramafic lamprophyre diatreme, Kenosha, Wisconsin, U.S.A. In: Institute on Lake Superior Geology, Annual Meeting, vol. 43. pp. 11–12.

Cathles, L.M., 1993. Oxygen isotope alteration in the Noranda mining district, Abitibi greenstone belt, Quebec. Econ. Geol. 88, 1483–1511. https://doi.org/10.2113/gsecongeo.88.6.1483.

Cernuschi, F., Dilles, J.H., Grocke, S.B., Valley, J.W., Kitajima, K., Tepley III, F.J., 2018. Rapid formation of porphyry copper deposits evidenced by diffusion of oxygen and titanium in quartz. Geology 46, 611–614 (doi: 10.1130#104C978).

Craddock, J.P., Malone, D.H., Porter, R., Compton, J., Luczaj, J., Konstantinou, A., Day, J.E., Johnston, S.T., 2017. Paleozoic reactivation structures in the Appalachian-Ouachita-Marathon foreland: far-field deformation across Pangea. Earth Sci. Rev. 169, 1–34. https://doi.org/10.1016/j.earscirev.2017.04.002.

de Ronde, C.E.J., 1995. Fluid chemistry and isotopic characteristics of seafloor hydrothermal systems and associated VMS deposits—potential for magmatic contributions. In: Thompson, J.F.H. (Ed.), Magmas, Fluids and Ore Deposits. 23. Mineralogical Association of Canada Short Course Series, Ottawa, Ontario, pp. 479–510.

DeMatties, T.A., 1996. A geologic framework for early Proterozoic volcanogenic massive sulfide deposits in Wisconsin: an exploration model. In: Volcanogenic Massive Sulfide Deposits of Northern Wisconsin: A Commemorative Volume. Institute on Lake Superior Geology, pp. 31–65.

Dewane, T.J., Van Schmus, W.R., 2007. U-Pb geochronology of the Wolf River Batholith, north-central Wisconsin: evidence for successive magmatism between 1484 Ma and 1468 Ma. Precambrian Res. 157, 215–234. https://doi.org/10.1016/j.precamres.2007.02.018.

Driese, S.G., Medaris Jr., L.G., 2008. Evidence for biological and hydrological controls on the development of a Paleoproterozoic paleoweathering profile in the Baraboo Range, Wisconsin, U.S.A. J. Sediment. Res. 787 (7), 443–457. https://doi.org/10.2110/jsr.2008.051.

Driesner, T., Seward, T.M., 2000. Experimental and simulation study of salt effects and pressure/density effects on oxygen and hydrogen stable isotope liquid-vapor fractionation for 4-5 molal aqueous NaCl and KCl solutions to 400 °C. Geochim. Cosmochim. Acta 64 (10), 1773–1784. https://doi.org/10.1016/S0016-7037(99)00435-4.

Franklin, J.M., Gibson, H.L., Jonasson, I.R., Galley, A.G., 2005. Volcanogenic massive sulfide deposits. In: Hedenquist, J.W., Thompson, J.F.H., Goldfarb, R.J., Richards, J.P. (Eds.), Economic Geology 100th Anniversary Volume. The Economic Geology Publishing Company, pp. 523–560.

Frape, S.K., Fritz, P., 1987. Geochemical trends for groundwaters from the Canadian Shield. In: Geological Association of Canada Special Paper. 33. pp. 19–38.

Friedman, I., O'Neil, J.R., 1977. Compilation of stable isotope fractionation factors of geochemical interest. In: Fleischer, M. (Ed.), Data of Geochemistry, Sixth edition. United States Geological Survey Professional Paper 440.

Graham, C.M., Valley, J.W., Winter, B.L., 1996. Ion microprobe analysis of $^{18}O/^{16}O$ in authigenic and detrital quartz in the St. Peter Sandstone, Michigan Basin and Wisconsin Arch, USA: Contrasting diagenetic histories. Geochimica et Cosmochimica Acta 60 (24), 5101–5116. https://doi.org/10.1016/s0016-7037(96)00286-4.

Haroldson, E.L., 2017. Protracted Development of the Reef Deposit: An Anomalous Au-Cu Deposit in Northern Wisconsin. PhD Dissertation. University of Wisconsin-Madison (175 p).

Haroldson, E.L., Beard, B.L., Satkoski, A.M., Brown, P.E., Johnson, C.M., 2018a. Gold remobilization associated with Mississippi Valley-type fluids: a Pb isotope perspective. Geol. Soc. Am. Bull. 130 (9–10), 1583–1595. https://doi.org/10.1130/B31901.1.

Haroldson, E.L., Brown, P.E., Bodnar, R.J., 2018b. Involvement of variably-sourced fluids during the formation and later overprinting of Paleoproterozoic Au-Cu mineralization: insights gained from a fluid inclusion assemblage approach. Chem. Geol. 497, 115–127. https://doi.org/10.1016/j.chemgeo.2018.08.027.

Hervig, R.L., Williams, P., Thomas, R.M., Schauer, S.N., Steele, I.M., 1992. Microanalysis of oxygen isotopes in insulators by secondary ion mass spectrometry. Int. J. Mass Spectrom. Ion Process. 120, 45–63. https://doi.org/10.1016/0168-1176(92)80051-2.

Heyl, A.V., Agnew, A.F., Lyons, E.J., Behre, C.H., Flint, A.E., 1959. The geology of the Upper Mississippi Valley zinc-lead district. In: United States Geological Survey Professional Paper 309, (310 p).

Holmden, C., Muehlenbachs, K., 1993. The $^{18}O/^{16}O$ ratio of 2-billion-year-old seawater inferred from ancient oceanic crust. Science 259 (5102), 1733–1736. https://doi.org/10.1126/science.259.5102.1733.

Horita, J., 2014. Oxygen and carbon isotope fractionation in the system dolomite–water–CO_2 to elevated temperatures. Geochim. Cosmochim. Acta 129, 111–124. https://doi.org/10.1016/j.gca.2013.12.027.

Horita, J., Cole, D.R., Wesolowski, D.J., 1993a. The activity-composition relationship of oxygen and hydrogen isotope in aqueous salt solutions: II. Vapor-liquid water equilibration of mixed salt solutions from 50 to 100°C and geochemical implications. Geochim. Cosmochim. Acta 57, 4703–4711. https://doi.org/10.1016/0016-7037(93)90194-2.

Horita, J., Wesolowski, D.J., Cole, D.R., 1993b. The activity-composition relationship of oxygen and hydrogen isotope in aqueous salt solutions: I. Vapor-liquid water equilibration of single salt solutions from 50 to 100°C. Geochim. Cosmochim. Acta 57, 2797–2817. https://doi.org/10.1016/0016-7037(93)90391-9.

Horita, J., Cole, D.R., Wesolowski, D.J., 1995. The activity-composition relationship of oxygen and hydrogen isotope in aqueous salt solutions: III. Vapor-liquid water equilibration of NaCl solutions to 350 °C. Geochim. Cosmochim. Acta 59 (6), 1139–1151. https://doi.org/10.1016/0016-7037(95)00031-T.

Hu, G., Clayton, R.N., 2003. Oxygen isotope salt effects at high pressure and high temperature and the calibration of oxygen isotope geochemistry. Geochim. Cosmochim. Acta 67 (17), 3227–3246. https://doi.org/10.1016/S0016-7037(02)01319-4.

Huston, D.L., Taylor, B.E., 1999. Genetic significance of oxygen and hydrogen isotope variations at the Kidd Creek volcanic-hosted massive sulfide deposit, Ontario, Canada. In: Economic Geology Monograph. 10. pp. 335–350.

Hyodo, A., Kozdon, R., Pollington, A.D., Valley, J.W., 2014. Evolution of quartz cementation and burial history of the Eau Claire Formation based on in situ oxygen isotope analysis of quartz overgrowth. Chem. Geol. 384, 168–180. https://doi.org/10.1016/j.chemgeo.2014.06.021.

Jaffrés, J.B.D., Shields, G.A., Wallmann, K., 2007. The oxygen isotope evolution of seawater: a critical review of a long-standing controversy and an improved geological water cycle model for the past 3.4 billion years. Earth Sci. Rev. 83, 83–122. https://doi.org/10.1016/j.earscirev.2007.04.002.

Kelly, J.L., Fu, B., Kita, N.T., Valley, J.W., 2007. Optically continuous silcrete quartz cements of the St. Peter Sandstone: high precision oxygen isotope analysis by ion microprobe. Geochim. Cosmochim. Acta 71 (15), 3812–3832. https://doi.org/10.1016/j.gca.2007.05.014.

Kennedy, L.P., Harding, T.A., 1990. Summary Report of the Reef Joint Venture. Noranda Exploration Inc., Marathon County, Wisconsin (63 p).

Kesler, S.E., Vennemann, T.W., Frederickson, C., Breithaupt, A., Vazquez, R., Furman, F.C., 1997. Hydrogen and oxygen isotope evidence for origin of MVT-forming brines, southern Appalachians. Geochim. Cosmochim. Acta 61 (7), 1513–1523. https://doi.org/10.1016/S0016-7037(97)00014-8.

Kita, N.T., Ushikubo, T., Fu, B., Valley, J.W., 2009. High precision SIMS oxygen isotope analysis and the effect of sample topography. Chem. Geol. 264, 43–57. https://doi.org/10.1016/j.chemgeo.2009.02.012.

Kozdon, R., Ushikubo, T., Kita, N.T., Spicuzza, M., Valley, J.W., 2009. Intratest oxygen isotope variability in the planktonic foraminifer N. pachyderma: real versus apparent vital effects by ion microprobe. Chem. Geol. 258, 327–337. https://doi.org/10.1016/j.chemgeo.2008.10.032.

Kutz, K.B., Spry, P.G., 1989. The genetic relationship between Upper Mississippi Valley district lead-zinc mineralization and minor base metal mineralization in Iowa, Wisconsin, and Illinois. Econ. Geol. 84, 2139–2154. https://doi.org/10.2113/gsecongeo.84.8.2139.

LaBerge, G.L., Myers, P.E., 1984. Two early Proterozoic successions in central Wisconsin and their tectonic significance. Geol. Soc. Am. Bull. 95 (2), 246–253. https://doi.org/10.1130/0016-7606(1984)95<246:TEPSIC>2.0.CO;2.

Leach, D.L., Taylor, R.D., Fey, D.L., Diehl, S.F., Saltus, R.W., 2010. A deposit model for Mississippi Valley-Type lead-zinc ores, chap. A of Mineral deposit models for resource assessment. U.S. Geological Survey Scientific Investigations Report 2010–5070–A 1–52.

Lentz, D.R., 1999. Petrology, geochemistry, and oxygen isotope interpretation of felsic volcanic and related rocks hosting the Brunswick 6 and 12 massive sulfide deposits (Brunswick belt), Bathurst mining camp, New Brunswick, Canada. Econ. Geol. 94, 57–86. https://doi.org/10.2113/gsecongeo.94.1.57.

Liu, J., Hay, R.L., Deino, A., Kyser, T.K., 2003. Age and origin of authigenic K-feldspar in uppermost Precambrian rocks in the North American Midcontinent. Geol. Soc. Am. Bull. 115 (4), 422–433. https://doi.org/10.1130/0016-7606(2003)115<0422:AAOOAK>2.0.CO;2.

Luczaj, J.A., 2006. Evidence against the Dorag (Mixing-Zone) model for dolomitization along the Wisconsin arch—a case for hydrothermal diagenesis. Am. Assoc. Pet. Geol. Bull. 90, 1719–1738. https://doi.org/10.1306/01130605077.

MacLean, W.H., Hoy, L.D., 1991. Geochemistry of hydrothermally altered rocks at the Horne Mine, Noranda, Quebec. Econ. Geol. 86, 506–528. https://doi.org/10.2113/gsecongeo.86.3.506.

O'Neil, J.R., Truesdell, A.H., 1991. Oxygen isotope fractionation studies of solute-water interactions. In: Stable Isotope Geochemistry: A Tribute to Samuel Epstein, The Geochemical Society Special Publication. 3. pp. 17–25.

Ohmoto, H., 1986. Stable Isotope Geochemistry of Ore Deposits. Reviews in Mineralogy and Geochemistry 16, 491–559.

Oliver, J., 1986. Fluids expelled tectonically from orogenic belts: Their role in hydrocarbon migration and other geologic phenomena. Geology 14 (2), 99–102. https://doi.org/10.1130/0091-7613(1986)14<99:FETFOB>2.0.CO;2.

O'Neil, J.R., Clayton, R.N., Mayeda, T.K., 1969. Oxygen isotope fractionation in divalent metal carbonates. J. Chem. Phys. 51 (12), 5547–5558. https://doi.org/10.1063/1.1671982.

Paradis, S., Taylor, B.E., Watkinson, D.H., Jonasson, I.R., 1993. Oxygen isotope zonation and alteration in the northern Noranda district, Quebec: evidence for hydrothermal fluid flow. Econ. Geol. 88, 1512–1525. https://doi.org/10.2113/gsecongeo.88.6.1512.

Pierson, B.J., 1981. The control of cathodoluminescence in dolomite by iron and manganese. Sedimentology 28, 601–610. https://doi.org/10.1111/j.1365-3091.1981.tb01924.x.

Pollington, A.D., Kozdon, R., Valley, J.W., 2011. Evolution of quartz cementation during burial of the Cambrian Mount Simon Sandstone, Illinois Basin: in situ microanalysis of $\delta^{18}O$. Geology 39 (12), 1119–1122. https://doi.org/10.1130/G32195.1.

Pollington, A.D., Kozdon, R., Anovitz, L.M., Georg, R.B., Spicuzza, M.J., Valley, J.W., 2016. Experimental calibration of silicon and oxygen isotope fractionations between quartz and water at 250 °C by in situ microanalysis of experimental products and application to zoned low $\delta^{30}Si$ quartz overgrowths. Chem. Geol. 421, 127–142. https://doi.org/10.1016/j.chemgeo.2015.11.011.

Schulz, K.J., Cannon, W.F., 2007. The Penokean orogeny in the Lake Superior region. Precambrian Res. 157, 4–25. https://doi.org/10.1016/j.precamres.2007.02.022.

Searl, A., 1988. The limitations of "cement stratigraphy" as revealed in some lower carboniferous oolites from South Wales. Sediment. Geol. 57, 171–183. https://doi.org/10.1016/0037-0738(88)90025-5.

Sharp, Z.D., Gibbons, J.A., Maltsev, O., Atudori, V., Pack, A., Sengupta, S., Shock, E.L., Knauth, L.P., 2016. Calibration of the triple oxygen isotope fractionation in the SiO_2–H_2O system and applications to natural samples. Geochim. Cosmochim. Acta 186, 105–119. https://doi.org/10.1016/j.gca.2016.04.047.

Sheppard, S.M.F., 1986. Characterization and isotopic variations in natural waters. In: Valley, J.W., Taylor Jr.H.P., O'Neil, J.R. (Eds.), Stable Isotopes in High Temperature Geological Processes. Mineralogical Society of America Reviews in Mineralogy 16. pp. 165–183.

Sherman, D.M., 2007. Complexation of Cu^+ in hydrothermal NaCl brines: ab initio molecular dynamics and energetics. Geochim. Cosmochim. Acta 71, 714–722. https://doi.org/10.1016/j.gca.2006.09.015.

Sims, P.K., Van Schmus, W.R., Schulz, K.J., Peterman, Z.E., 1989. Tectono-stratigraphic evolution of the Early Proterozoic Wisconsin magmatic terranes of the Penokean Orogen. Can. J. Earth Sci. 26, 2145–2158. https://doi.org/10.1139/e89-180.

Śliwiński, M.G., Kitajima, K., Kozdon, R., Spicuzza, M.J., Fournelle, J.H., Denny, A., Valley, J.W., 2016a. Secondary ion mass spectrometry bias on isotope ratios in dolomite–ankerite, part I: $\delta^{18}O$ matrix effects. Geostand. Geoanal. Res. 40, 157–172. https://doi.org/10.1111/j.1751-908X.2015.00364.x.

Śliwiński, M.G., Kozdon, R., Kitajima, K., Denny, A., Valley, J.W., 2016b. Microanalysis of carbonate cement $\delta^{18}O$ in a CO_2-storage system seal: insights into the diagenetic history of the Eau Claire Formation (Upper Cambrian), Illinois Basin. Am. Assoc. Pet. Geol. Bull. 100 (6), 1003–1031. https://doi.org/10.1306/02031615065.

Smith, G.L., Simo, J.A., 1997. Carbonate diagenesis and dolomitization of the Lower Ordovician Prairie du Chien Group. Geosci. Wis. 16, 1–16.

Spicuzza, M.J., Valley, J.W., Kohn, M.J., Girard, J.P., Fouillac, A.C., 1998. The rapid heating, defocused beam technique: a CO_2-laser based method for highly precise and accurate determination of $\delta^{18}O$ values of quartz. Chem. Geol. 144, 195–203. https://doi.org/10.1016/S0009-2541(97)00131-9.

Spirakis, C.S., Heyl, A.V., 1996. Fracturing radioactive basement rocks as the energy source to drive mineralization in the Upper Mississippi Valley zinc-lead district. Soc. Econ. Geol. Spec. Publ. (4), 390–399.

Stipp, M., Stünitz, H., Heilbronner, R., Schmid, S., 2002a. Dynamic recrystallization of quartz: correlation between natural and experimental conditions. Geol. Soc. Lond., Spec. Publ. 200, 171–190. https://doi.org/10.1144/GSL.SP.2001.200.01.11.

Stipp, M., Stünitz, H., Heilbronner, R., Schmid, S., 2002b. The eastern Tonale fault zone: a 'natural laboratory' for crystal plastic deformation of quartz over a temperature range from 250 to 700 °C. J. Struct. Geol. 24, 1861–1884. https://doi.org/10.1016/S0191-8141(02)00035-4.

Taylor Jr., H.P., 1979. Oxygen and hydrogen isotope relationships in hydrothermal mineral deposits. In: Barnes, H.L. (Ed.), Geochemistry of Hydrothermal Ore Deposits. Wiley-Intersci, New York, pp. 236–277.

Truesdell, A.H., 1974. Oxygen isotope activities and concentrations in aqueous salt solutions at elevated temperatures: consequences for isotope geochemistry. Earth Planet. Sci. Lett. 23, 387–396. https://doi.org/10.1016/0012-821X(74)90128-9.

Valley, J.W., Kita, N.T., 2009. In situ oxygen isotope geochemistry by ion microprobe. In: Fayek, M. (Ed.), Secondary Ion Mass Spectrometry in the Earth Sciences. 41. Mineralogical Association of Canada Short Course, pp. 19–63.

Valley, J.W., Kitchen, N.E., Kohn, M.J., Niendorf, C.R., Spicuzza, M., 1995. UWG-2, a garnet standard for oxygen isotope ratios: strategies for high precisions and accuracy with laser heating. Geochim. Cosmochim. Acta 59, 5223–5231.

Van Schmus, W.R., Hinze, W.J., 1985. The midcontinent rift system. Annual Review of Earth and Planetary Science 13, 345–383. https://doi.org/10.1146/annurev.ea.13.050185.002021.

Voss, R.L., Hagni, R.D., Gregg, J.M., 1989. Sequential deposition of zoned dolomite and its relationship to sulfide mineral paragenetic sequence in the Viburnum trend, southeast Missouri. Carbonates Evaporites 4 (2), 195–209. https://doi.org/10.1007/BF03175107.

Wang, X.-L., Coble, M.A., Valley, J.W., Shu, X.-J., Kitajima, K., Spicuzza, M.J., Sun, T., 2014. Influence of radiation damage on Late Jurassic zircon from southern China: evidence from in situ measurements of oxygen isotopes, laser Raman, U-Pb ages, and trace elements. Chem. Geol. 389, 122–136. https://doi.org/10.1016/j.chemgeo.2014.09.013.

Whitmeyer, S.J., Karlstrom, K.E., 2007. Tectonic model for the Proterozoic growth of North America. Geosphere 3 (4), 220–259. https://doi.org/10.1130/GES00055.1.

Wilkinson, M., Crowley, S.F., Marshall, J.D., 1992. Model for the evolution of oxygen isotope ratios in the pore fluids of mudrocks during burial. Mar. Pet. Geol. 9 (1), 98–105. https://doi.org/10.1016/02648172(92)90007-2.

Zartman, R.E., Kempton, P.D., Paces, J.B., Downes, H., Williams, I.S., Dobosi, G., Futa, K., 2013. Lower-crustal xenoliths from Jurassic kimberlite diatremes, Upper Michigan (USA): evidence for Proterozoic orogenesis and plume magmatism in the lower crust of the southern Superior Province. J. Petrol. 54 (3), 575–608. https://doi.org/10.1093/petrology/egs079.